



Nonthermal Radio Continuum Emission from Young Nearby Stars

Ralf Launhardt¹ , Laurent Loinard^{2,3} , Sergio A. Dzib⁴ , Jan Forbrich^{5,6} , Geoffrey C. Bower⁷ , Thomas K. Henning¹ ,Amy J. Mioduszewski⁸, and Sabine Reffert⁹ ¹ Max-Planck-Institut für Astronomie, Königstuhl 17, D-69117 Heidelberg, Germany; rl@mpia.de² Instituto de Radioastronomía y Astrofísica, Universidad Nacional Autónoma de México, Apartado Postal 3-72, 58090, Morelia, Michoacán, Mexico³ Instituto de Astronomía, Universidad Nacional Autónoma de México, Apartado Postal 70-264, Ciudad de México 04510, Mexico⁴ Max-Planck-Institut für Radioastronomie, Auf dem Hügel 69, D-53121 Bonn, Germany⁵ Centre for Astrophysics Research, University of Hertfordshire, College Lane, Hatfield AL10 9AB, UK⁶ Center for Astrophysics | Harvard & Smithsonian, 60 Garden Street, Cambridge, MA 02138, USA⁷ Academia Sinica Institute of Astronomy and Astrophysics, 645 N. A'ohoku Place, Hilo, HI 96720, USA⁸ National Radio Astronomy Observatory, Array Operations Center, 1003 Lopezville Road, Socorro, NM 87801, USA⁹ Landessternwarte, Zentrum für Astronomie der Universität Heidelberg, Königstuhl 12, D-69117, Heidelberg, Germany

Received 2022 January 20; revised 2022 March 3; accepted 2022 March 3; published 2022 May 23

Abstract

Young and magnetically active low-mass stars often exhibit nonthermal coronal radio emission owing to the gyration of electrons in their magnetized chromospheres. This emission is easily detectable at centimeter wavelengths with the current sensitivity of large radio interferometers like the Very Large Array (VLA). With the aim of identifying nearby stars adequate for future accurate radio astrometric monitoring using very long baseline interferometry (VLBI), we have used the VLA in its B configuration to search for radio emission at $\nu \simeq 6$ GHz ($\lambda \simeq 5$ cm) toward a sample of 170 nearby (<130 pc), mostly young (5–500 Myr) stars of spectral types between F4 and M2. At our mean 3σ detection limit of $\simeq 50$ μ Jy, we identify 31 young stars with coronal radio emission (an 18% system detection rate) and more than 600 background (most likely extragalactic) sources. Among the targeted stars, we find a significant decline of the detection rate with age from $56\% \pm 20\%$ for stars with ages ≤ 10 Myr to $10\% \pm 3\%$ for stars with ages 100–200 Myr. No star older than 200 Myr was detected. The detection rate also declines with T_{eff} from $36\% \pm 10\%$ for stars with $T_{\text{eff}} < 4000$ K to $13\% \pm 3\%$ for earlier spectral types with $T_{\text{eff}} > 5000$ K. The binarity fraction among the radio-bright stars is at least twice as high as among the radio-quiet stars. The radio-bright nearby young stars identified here provide an interesting sample for future astrometric studies using VLBI arrays aimed at searching for hitherto-unknown tight binary components or even exoplanets.

Unified Astronomy Thesaurus concepts: Galactic radio sources (571); Radio interferometry (1346); Pre-main sequence stars (1290); Non-thermal radiation sources (1119)

Supporting material: figure set

1. Introduction

Young low-mass stars are often magnetically and chromospherically active owing to their convective envelopes that enable dynamo processes (Bouvier et al. 2014). One of the many possible manifestations of this activity is the existence of coronal radio emission detectable at centimeter wavelengths. Such radio emission is typically highly variable with flares and is largely accepted to result from the gyration of electrons in dynamo-driven stellar magnetic fields (Dulk 1985; Feigelson & Montmerle 1985; Güdel 2002). Gyrosynchrotron radiation, where the population of electrons is mildly relativistic, seems to be the most common situation, but maser-amplified cyclotron emission (where the electrons are nonrelativistic) and synchrotron radiation (associated with highly relativistic electrons) have been suggested in a few cases (Dzib et al. 2010; Deller et al. 2013). Regardless of the exact emission mechanism, the emission is normally

confined to regions extending at most a few stellar radii (Smith et al. 2003; Massi et al. 2006; Torres et al. 2012), making high-resolution very long baseline interferometry (VLBI) observations of coronal radio emission a powerful tool to study the astrometry of low-mass young stars (e.g., Ortiz-León et al. 2017a; Dzib et al. 2021). Furthermore, milliarcsecond-resolution VLBI observations would efficiently filter out any possible thermal free-free contribution to the radio fluxes, since even faint detections will have corresponding brightness temperatures of several $\times 10^6$ K (Forbrich et al. 2021).

The Gould Belt Very Large Array survey of nearby regions (Loinard et al. 2011; Dzib et al. 2013; Kounkel et al. 2014; Dzib et al. 2015; Ortiz-León et al. 2015; Pech et al. 2016) has shown that, with the current level of sensitivity reachable in large-scale surveys ($\sigma \approx 20$ μ Jy), the fraction of young stellar objects (YSOs) with coronal emission that can be detected at radio wavelengths is of order 10%–30% in regions of ongoing star formation located within a few hundred parsecs around the Sun, such as Taurus, Ophiuchus, or Perseus. In such regions, the most frequently detected stars with coronal radio emission are young, but no longer



Original content from this work may be used under the terms of the [Creative Commons Attribution 4.0 licence](https://creativecommons.org/licenses/by/4.0/). Any further distribution of this work must maintain attribution to the author(s) and the title of the work, journal citation and DOI.

embedded, Class III weak-line T Tauri stars (TTs) of spectral types K and earlier, but also somewhat younger Class II classical TTs, often with IR excess originating from circumstellar disks.¹⁰

Although it has been shown that nonthermal (coronal) radio emission is predominantly detected toward low-mass (spectral types M, K, and G) Class II classical TTs and Class III weak-line TTs (e.g., Pech et al. 2016), little is known empirically about the evolution with age of coronal radio emission. Theoretically, such emission is expected to decrease with age, since it depends on the stellar magnetic activity, which in turn is linked to a stellar rotation period that increases on a timescale of a few hundred megayears owing to magnetic braking (e.g., Güdel 2002, 2004; Bouvier et al. 2014). Thus, it remains to be shown how frequently weak-lined TTs with ages between 10 and a few hundred megayears exhibit strong coronal emission and if the emission indeed declines on that timescale.

In this article, we present the results of a survey for coronal radio emission from young low-mass stars in the immediate solar neighborhood at distances between 8 and 130 pc, i.e., inside the Local Bubble (Zucker et al. 2022) and the Gould Belt, and thus complementary to the Gould Belt Very Large Array survey. The ultimate goal of our survey was to identify suitable target stars for an anticipated astrometric planet search with the Very Long Baseline Array (VLBA; see, e.g., Bower et al. 2009; Curiel et al. 2020). At the same time, our survey investigates systematically, for the first time, the coronal radio emission from the most nearby young solar-mass stars around the Sun.

The paper is structured as follows. In Section 2, we introduce the target selection and source list of our survey. Section 3 describes the Karl G. Jansky Very Large Array (VLA) observations and data reduction. The results of the survey are presented in Section 4, and the relation between radio emission and stellar properties is discussed in Section 5. Finally, the paper is summarized in Section 6.

2. Target Selection and Source List

Due to the findings about the coronal gyro-synchrotron radio emission mentioned above and our goal of identifying targets for an anticipated astrometric planet search, we restricted our source list to stars within 130 pc around the Sun (based on Hipparcos parallaxes) that have published age estimates below 300 Myr and to stars with roughly solar masses in the spectral range late K to mid-F. Due to the latitude distribution of the VLBA telescopes (for the anticipated astrometric monitoring), we further restricted the sample to targets with decl. $\geq -20^\circ$. Finally, we rejected known spectroscopic binaries for which the later astrometric analysis would be complicated or even impossible. In some individual cases, where, e.g., the distance or spectral type had a nonnegligible uncertainty, the boundaries of these selection criteria were not applied very strictly.

With these selection criteria, we have compiled our target list from the body of literature devoted to the kinematics of young stars in the solar neighborhood (Montes et al. 2001;

Wichmann et al. 2003; Zuckerman & Song 2004; López-Santiago et al. 2006; da Silva et al. 2009; Montes et al. 2009; Maldonado et al. 2010; Zuckerman et al. 2011; Nakajima & Morino 2012) and studies of the evolution of protoplanetary disks and debris disks (Meyer et al. 2006; Carpenter et al. 2009). The resulting list contains in total 220 stars, of which 169 stars were observed with the VLA. The remaining ≈ 50 stars in the R. A. range 17.5 ± 2 hr could not be scheduled for observations owing to oversubscription of the Galactic center R.A. range.

While the original target selection was based on the criteria and resources described above, we later reevaluated the stellar effective temperatures, T_{eff} , distances, d , and ages, t_* . T_{eff} was derived by fitting simultaneous stellar (PHOENIX; Husser et al. 2013) and blackbody models (to account for disk excess emission where present) to the observed photometry and spectra as described in Launhardt et al. (2020). The distances are rederived from the Gaia-DR2 (hereafter GDR2) parallaxes (Gaia Collaboration et al. 2018) according to the formalism described by Bailer-Jones et al. (2018). For four targets, which have no valid GDR2 parallax solutions, distances are derived by other means as indicated in Table 3.

To reevaluate the stellar ages, we first checked each target for membership of known young associations (moving groups) using the banyan Σ tool¹¹ (Gagné et al. 2018). If the membership probability was $\geq 80\%$, then we assigned the stellar age t_* to be the mean age of the association.¹² In addition, we adopted association ages for 31 more targets that were identified by other authors (Montes et al. 2001; da Silva et al. 2009, and others) as likely association members. In total we thus assigned association ages to 99 of our 169 observed target stars. For the remaining 70 field stars, ages were assigned by compiling various literature estimates (particularly from large surveys with diverse age-determination methods; e.g., Stanford-Moore et al. 2020). If multiple valid age estimates were available, then we adopted an age (and conservative uncertainty range) that accounted for the spread in estimates.

The complete list of observed stars with their basic properties is compiled in Table 3. Stars with VLA detections are marked in boldface. Figure 1 shows the distributions of T_{eff} stellar effective temperatures and corresponding spectral types, ages, distances, and V magnitudes of all observed and detected stars. Figure 2 shows a $V-K$ color-magnitude diagram (CMD) of the target stars, also with the 6 GHz detections marked. It can already be seen in both figures that nearly all VLA-detected stars are young (< 200 Myr) and lie above the main sequence, but these correlations are discussed in more detail in Section 5.2. Stellar effective temperatures T_{eff} range from 3000 to 6700 K (one outlier with 10,000 K), with a median of 5315 K. Spectral types range from F4 to M2, with a median of G8. Distances range from 8 to 400 pc, with a median of 43 pc, and with only six stars having distances > 130 pc. Visual magnitudes range from 3 to 13.8 mag, with a median of 8.6 mag. Ages range from $\lesssim 5$ Myr¹³ to 12 Gyr, with a median of 149 Myr. Other than anticipated in our original target selection, our list now contains 25 stars with ages > 500 Myr, which actually serve as a nice comparison group (see discussion in Section 5.2).

¹⁰ Note that YSOs, especially when at earlier evolutionary stages (Class 0 and I), can also emit at radio wavelengths because of thermal free-free emission associated with shock-ionized material in, e.g., jets, winds, or accretion flows (e.g., André et al. 1987; Anglada et al. 1992; Eisloffel et al. 2000; Anglada et al. 2018). We may not always be able to disentangle these mechanisms, and they can also occur simultaneously. However, these mechanisms are not considered here, as they require the presence of dense circumstellar material, not expected to be present in stars with ages larger than a few megayears.

¹¹ <http://www.exoplanetes.umontreal.ca/banyan/banyansigma.php>

¹² For five stars with membership probabilities between 55% and 75%, we also assigned the mean age of the association because these ages are widely used in the literature. These stars are marked in Table 3.

¹³ Because of the uncertainties involved, we treat the age of the TAU association, 1–2 Myr (Kenyon & Hartmann 1995; Gagné et al. 2018), as $\lesssim 5$ Myr.

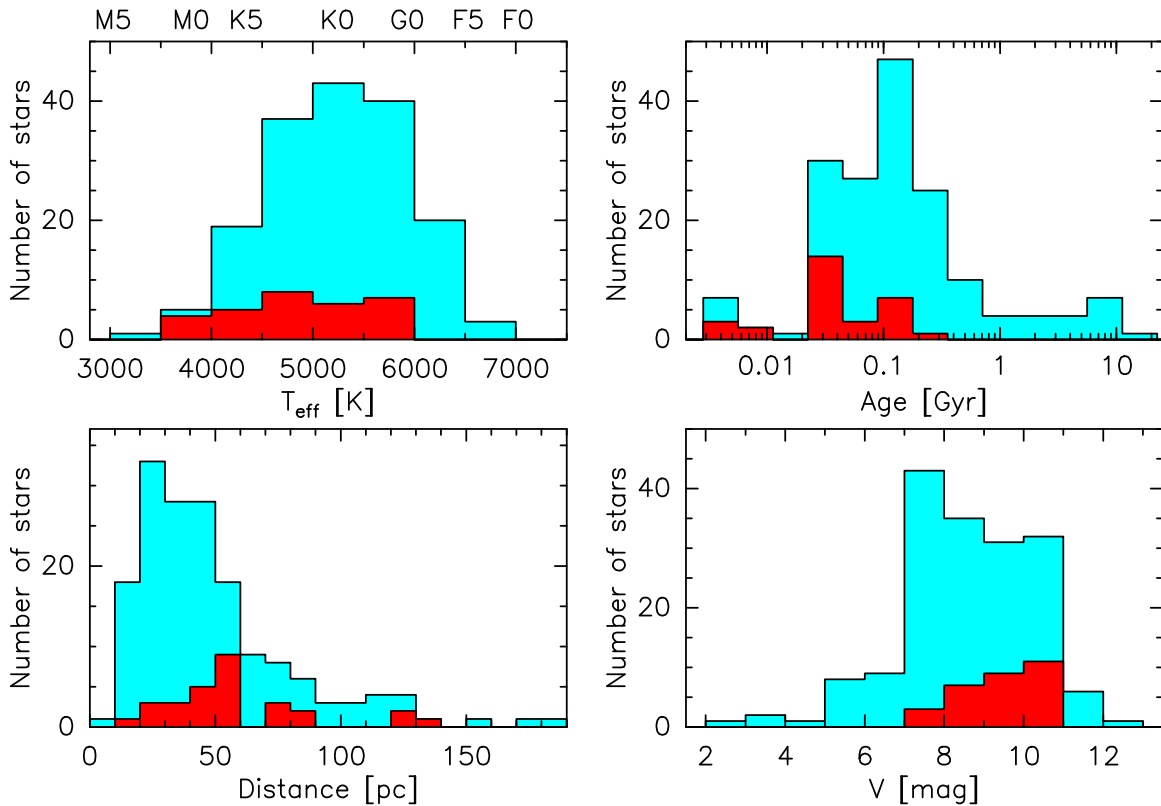


Figure 1. Distribution of stellar effective temperatures, ages, distances, and V magnitudes for the observed (light-blue histograms) and detected (at 6 GHz) stars (red histograms).

Nearly all of our targets have IR ($2.2\text{--}22\ \mu\text{m}$; from Two Micron All Sky Survey (2MASS) and WISE) spectral indices $\alpha = \frac{d \log(\lambda F_\lambda)}{d \log(\lambda)}$ between -3.0 and -2.4 (mean -2.8 ± 0.2), i.e., they are Class III sources (Adams et al. 1987; Lada 1987) and correspond roughly to weak-line TTSs that no longer possess protoplanetary disks. However, about 20 of our 169 observed targets have detected (mostly by Herschel) far-IR excesses longward of $50\ \mu\text{m}$, most likely indicative of cold debris disks.

3. Observations and Data Reduction

Observations were carried out with the VLA of the National Radio Astronomy Observatory (NRAO) in its B configuration between 2013 October and 2014 January (project 13B-111). The C -band receivers were used with dual polarization and two sub-bands, each 1 GHz wide and centered at 5.5 and 6.5 GHz, respectively, thus providing a total bandwidth of 2 GHz. The primary beam FWHM size (field of view (FOV)) of the VLA antennas at 6 GHz ($\lambda \approx 5\ \text{cm}$) is $7''.5$. The mean synthesized FWHM beamwidth (angular resolution) of the VLA B configuration at 6 GHz is $\approx 2''.0$ (major axis). For low-elevation targets the major axis is $\approx 3''.5$.

In total we observed 169 target stars with 162 pointings (i.e., seven pointings had two target stars in one field), grouped in six 2 hr sessions with 25–30 pointings per session. The integration time per field was 165 s. Each observing session started with a 10-minute integration on a suitable standard flux calibrator. Then followed a series of observations of typically three to four target fields located close together on the sky, bracketed by 1–2 minutes of integrations on a phase calibrator that was located within 10° from all target fields in that group. To ensure that we also obtain a measure of the long-term flux variability, each session was repeated, with the two

observations separated by 1 to a few weeks. One short extra session with three stars could be scheduled only once. Thus, we observed 166 stars twice, and three more stars could be observed only once. The individual observing session parameters are summarized in Table 1.

The data were reduced using the VLA Calibration Pipeline as implemented in the Common Astronomy Software Applications package (CASA). In a nutshell, the pipeline determines the complex gains using the observations of the calibrators and transfers them to the target sources. It also automatically flags some radio frequency interferences (RFIs), but we did additional flagging by hand. In particular, one of the lower-frequency spectral windows had to be flagged entirely, as it contained strong RFIs that rendered it useless. After calibration, the data were imaged (also in CASA). The entire FOV ($7''.5$) was reconstructed in each field, and sources were searched systematically over the entire area mapped. The noise level in the final images was typically $15\text{--}20\ \mu\text{Jy beam}^{-1}$. The probability that a noise peak exceeds 5σ is 3×10^{-7} . There are roughly 16,500 independent resolution elements in each of our images. Thus, for each individual field, there is only a 0.5% chance that a noise peak above 5σ exists. Accounting for the fact that we observed 162 fields in total, we expect at most one false positive.

Source identification was done by visually inspecting the images. First, the regions near the known positions of targeted YSOs were examined. Then, we looked for additional sources in the entire field. Positions, integrated fluxes, and peak flux densities of each source were obtained by fitting an elliptical Gaussian in a small region containing the source. The elliptical Gaussian is adequate for both unresolved and only slightly resolved sources, as is the case for the expected emission of our targeted YSOs. Typical (median) positional uncertainties of the Gaussian fit

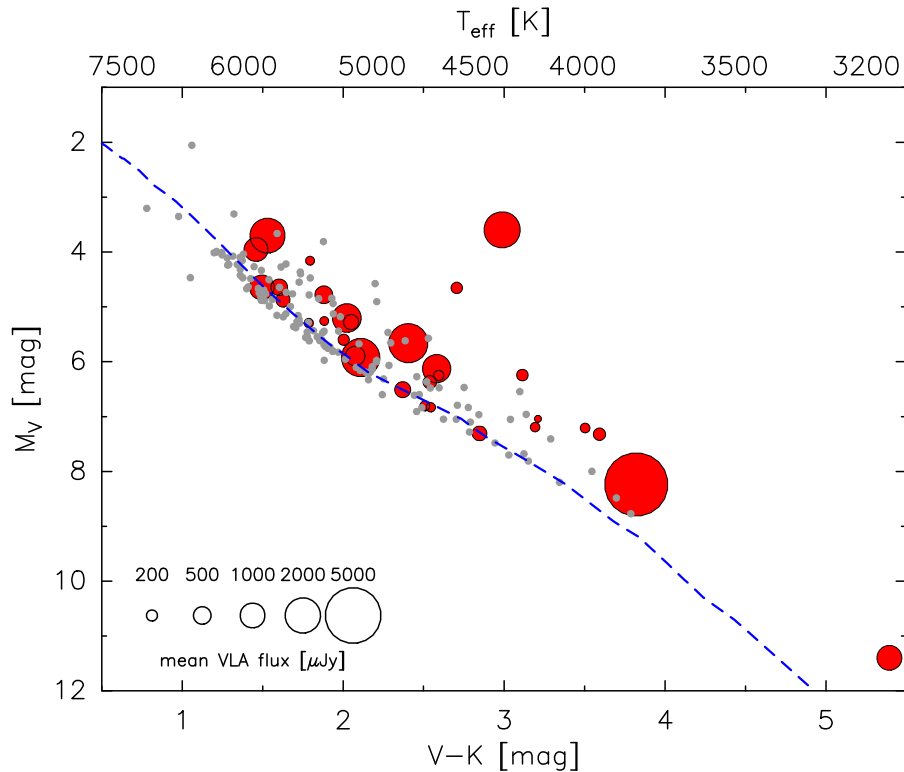


Figure 2. CMD of observed target stars. Nondetected stars (at 6 GHz) are marked by gray circles; detected stars are marked by filled red circles. The symbol size scales with the mean VLA flux following the scale displayed in the lower left corner. To guide the eye, the main sequence from Pecaut & Mamajek (2013) is marked by a dashed blue curve, and the effective temperatures corresponding to the $V - K$ color of main-sequence stars are marked on top.

Table 1
VLA Observing Sessions

Session	No. of Pointings	No. of Stars	Duration	Obs 1 Date	Obs 2 Date
1	27	30	2:00	2013-10-29	2013-11-16
2	28	30	2:00	2013-10-30	2013-11-6
3	30	31	2:00	2013-11-17	2013-12-1
4	20	21	1:45	2013-11-25	2014-01-3
5	27	28	2:00	2013-11-27	2013-12-30
6 ^a	25	25
7	26	26	2:00	2013-10-29	2013-11-17
8 ^b	3	3	0:30	2014-01-10	...

Notes.

^a Session 6 was not scheduled owing to oversubscription in the Galactic center R.A. range.

^b Session 8 was a short filler to use the remaining granted time and could not be repeated.

centers are 140 mas in R.A. and 190 mas in decl. for the entire sample of VLA detections, and 70–80 mas, respectively, for the detections associated with target stars (because these are on average brighter than the unrelated VLA detections; see Section 4.1 and Figure 3). The typical uncertainty in estimated flux densities is 20% for the entire sample and 7% for the detections associated with target stars.

4. Results

4.1. Overview of 6 GHz Detections

In total, we have identified 1287 6 GHz radio sources in the 162 fields observed, of which 1252 sources (97.3%) are

significant with signal-to-noise ratio (S/N) ≥ 3 (1181 sources or 91.8% with $S/N \geq 5$). Figure 3 shows the distribution of S/N versus peak flux for all identified 6 GHz radio sources. Note that many (but not all) sources may have been detected in both respective observing epochs. We did not check this epoch crossmatch for the full list of detections, but instead first identified associations between radio sources and target stars and then worked out the epoch crossmatch only on those radio sources that are likely associated with (known) stars. Thus, the actual number of physical radio sources in the observed fields is smaller than 1252, but still ≥ 626 .

As a first step toward identifying possible radio counterparts to our target stars, we used the 2MASS positions (Skrutskie et al. 2003), which are available for all our targets,¹⁴ together with the respective newest proper-motion values we could obtain (see Section 4.2). For each target star, we then calculated the expected position and positional uncertainty at the mid-epoch of the VLA observations and determined the angular separation and its uncertainty to the nearest VLA source. The separation uncertainty is derived from the uncertainties of the predicted star position and of the VLA position. The first one is determined by both the formal uncertainty of the 2MASS positions and the uncertainty of the proper motion multiplied by the time between the respective 2MASS and VLA observing epochs. The latter one is derived by adding in quadrature the formal image fitting positional uncertainty of the VLA source (see Section 3), the formal uncertainty of the respective phase calibrator positions as listed in the VLA calibrator catalog, and a fixed term of 10 mas (conservative estimate) for phase errors during the observations (see Section 4.2). The median

¹⁴ At the time of this assessment, GDR2 was not yet released.

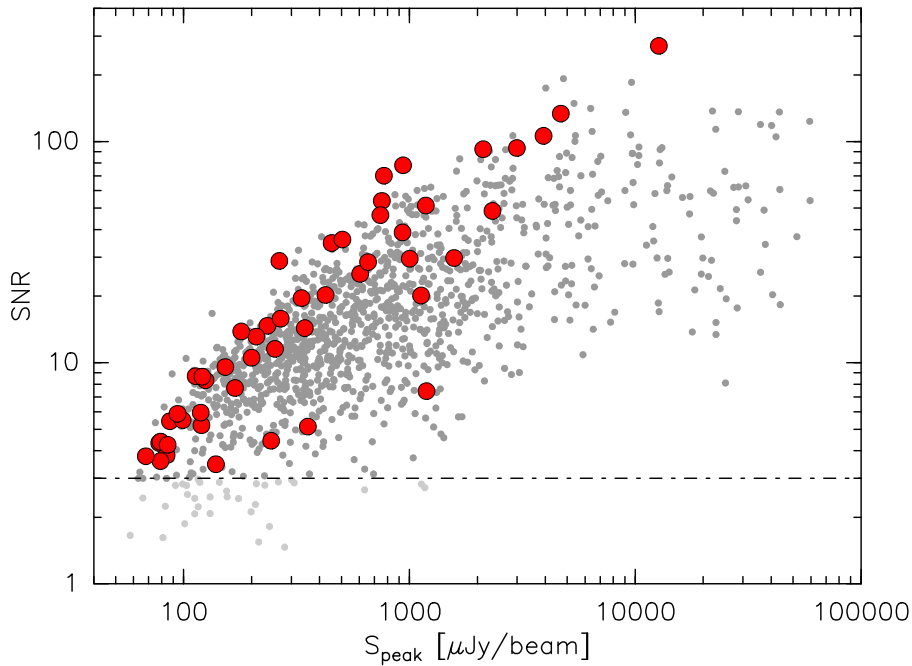


Figure 3. Distribution of S/N vs. peak flux for all 1287 identified 6 GHz radio sources (small gray circles). The horizontal dashed–dotted line indicates $S/N = 3\sigma$, the threshold above which we consider the radio detections significant (darker-gray circles). Large red circles indicate those VLA detections with $S/N \geq 3$ within $r \leq 6''$ (see Figure 4) around the predicted positions of a target star that we consider as potential detection of the target star.

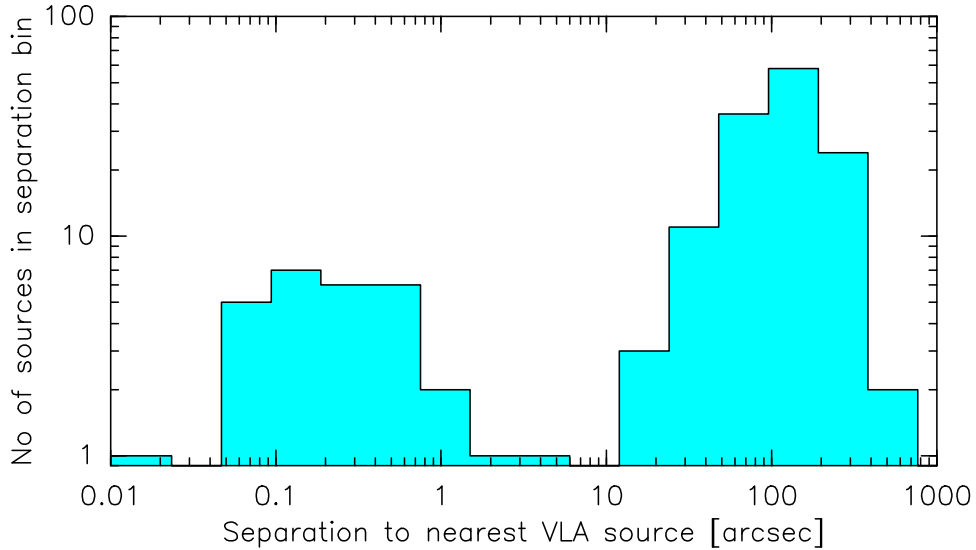


Figure 4. Number of target stars as a function of angular separation between the position predicted (from the 2MASS position and the proper motion) and the nearest VLA source (Section 4.1). Note that the separation bins are logarithmic.

separation uncertainty (between the predicted optical and the observed radio position) is ≈ 150 mas, with an rms scatter of ≈ 180 mas.

Figure 4 shows the resulting histogram of the number of target stars as a function of angular separation between predicted star position and the nearest VLA source with logarithmic separation bins. The distribution of nearest-neighbor separations is clearly bimodal, with the first peak located at a few tenths of an arcsecond and the second, much broader peak centered at a separation of $\approx 100''$ – $200''$. The first peak encompasses 30 target stars, with 28 stars having VLA detections within $< 1''$ and only two stars having nearest VLA detections at separations $1''$ – $5''$. The second peak contains the remaining 139 target stars with nearest VLA detections at

separations $> 12P''$. There is no target star with nearest VLA detection between $5''$ and $12''$. Given the positional uncertainties and the typical angular separations of (potential) physically bound companions, plus the clear bimodality of the nearest-neighbor separation distribution, it is safe to consider all 139 target stars with nearest-neighbor VLA sources at separations $> 10''$ not to exhibit detectable radio emission (at the time of the observations). For the 30 target stars with nearest-neighbor VLA detections within $5''$, we also checked whether a second-nearest VLA neighbor was located closer than $10''$, but we found none.

To evaluate whether any of the ≈ 1200 VLA radio sources that are not related to our target stars might be related to other, not targeted stars, we carried out a SIMBAD query with a

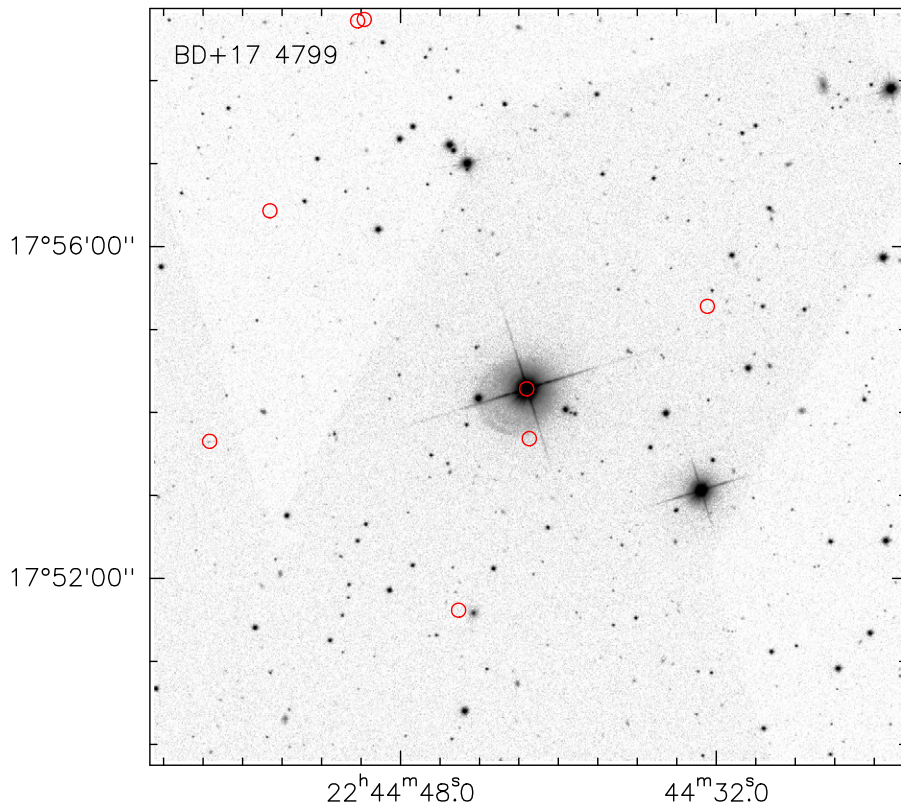


Figure 5. SDSS r -band image of a field around the target star BD +17 4799. Overlaid as red open circles are the positions of all eight VLA radio sources detected in this field.

search radius of $6''$. This search radius was motivated by the 2MASS-based separation distribution between stars and nearest VLA source shown in Figure 4. The choice of an angular search radius, as opposed to an absolute one, is justified by the fact that we are looking for physical associations with discrepancies mainly originating from proper-motion and pointing uncertainties and by the clear separation and large gap size between the two separation distribution groups (Figure 4). This search resulted in matches for only 175 out of the 1252 VLA sources. Of these, 117 matches are known galaxies, QSOs, or just listed radio sources with a nonidentified optical counterpart. The most frequent associations were found in the NRAO VLA Sky Survey (NVSS; Condon et al. 1998) and in the Lyon-Meudon Extragalactic Database (LEDA; Paturel et al. 1995).

Only 58 VLA sources are related to known stars, of which 53 are related to the 30 target detection candidates mentioned above and described in more detail in Section 4.2. Note that VLA detections in separate epochs or overlapping fields are all counted separately, such that the number of counted VLA sources is always larger than the number of physical sources to which they are related. Only five additional (out of the 58) VLA sources are located within $6''$ around two nontargeted stars. Three of these VLA detections (in two epochs and two fields) are located $5''.6$ away from HIP 14807 (BD +21 418B) at 03:11:12.334, +22:25:22.73. However, based on an astrometric analysis as described in Section 4.2, the VLA source does not seem to be associated with the star. It is most likely an unrelated background source. The other two VLA detections are related to UCAC 4 832–014013 at 15:07:57.226, +76:13:59.15, which is a high-proper-motion M4.5 star at a distance of ~ 30 pc (Table 3). A VLA radio source was detected

in both epochs at $0''.19$ from the predicted ICRS position of this star. The astrometric analysis confirmed that we have indeed detected radio emission from this star (Section 4.2). Thus, 55 out of our 1252 VLA detections are related to 31 (known) stars.

We conclude that 31 of the observed 169+1 target stars (not counting companions) are potentially associated with 6 GHz radio emission above the mean 3σ detection limit of $\approx 45 \mu\text{Jy}$. This would correspond to a detection rate of $18\% \pm 3\%$ if all stars were single. Since this is not the case, we convert this system detection rate into a star detection rate in Section 5.4. Of these, 22 sources were detected in two epochs, eight sources were detected in only one out of two epochs, and one detected object was observed only once. Figure 3 shows that the vast majority of the detection candidates line up at the upper envelope of the S/N versus peak flux distribution of detected radio sources, i.e., they are all significant. This is most likely related to the fact that the stars are nearly always located at the pointing centers, where the sensitivity is highest, while many of the other detections in the respective fields are located farther out in the FOV of the synthesized beams, where the sensitivity is lower. To determine whether the detection candidates are indeed associated with the target stars, or whether they could possibly also be related to known or unknown (stellar) companions, we investigate all 31 detection candidates astrometrically in more detail in Section 4.2.

Based on the analysis outlined above, we conclude that all 1197 (1252–55) radio sources not associated with known stars (96%) are likely related to background sources (galaxies, quasars) at cosmological distances. This is nicely illustrated by Figure 5, which shows as one example a Sloan Digitized Sky Survey (SDSS; red) image (York et al. 2000) of the target star SAO 108142 (= BD +17 4799) overlaid with the positions of

all eight 6 GHz radio sources detected in this field. Apart from the VLA source at the target star position, none of the other radio sources are positionally associated with a visible star. Only one source at $\approx 22:44:57.7 + 17:53:30$ (Figure 5, center left) is associated with a very faint and fuzzy (i.e., not point-like) optical counterpart, but a SIMBAD search only lists the not further described radio source NVSS J224457+175338 at this position. Since we are interested in radio emission from nearby young stars only, we do not further follow up or discuss these apparently unrelated radio sources, nor do we investigate which ones in the two epochs may be related to the same physical source. However, we note that with ≥ 616 supposedly extragalactic background sources in 162 fields with 7.5 diameter (Section 3), we observe a surface density of ≈ 0.1 sources arcmin^{-2} with a flux density at 6 GHz greater than $\approx 50 \mu\text{Jy}$. This compares well with the results of Fomalont et al. (1991), who predict a surface density of 0.2 ± 0.1 background sources arcmin^{-2} at the $50 \mu\text{Jy}$ detection threshold.

4.2. Astrometric Association of VLA Sources with Known Stars

To verify the physical association of the 31 VLA detection candidates with the target stars, we evaluate position measurements and proper-motion predictions from up to four additional catalogs (besides the VLA measurements), thus covering observing epochs from 1991.25 (Hipparcos) to 2015.5 (GDR2). In particular, we evaluate the following catalogs, for which we also list the epoch (or epoch range) and the typical (mean) positional uncertainty, σ_{pos} :

1. Hipparcos, the New Reduction (van Leeuwen 2010), $E_p = 1991.25$ (JD 2,448,349.0625), $\sigma_{\text{pos}} \approx 1$ mas. For targets with no entry in this catalog, we use the positions, proper motions, and individual epochs from the Tycho2 catalog (Høg et al. 2000) instead.
2. 2MASS (Skrutskie et al. 2003), epochs for individual data sets 1997–2000 (JD 2,450,727–2,451,875 for our targets), $\sigma_{\text{pos}} \approx 80$ mas.
3. WISE (Cutri et al. 2012), default mid-epoch of WISE coordinates = 2010.5589 (JD 2,455,400.63889), $\sigma_{\text{pos}} \approx 37$ mas.
4. VLA observations between 2013 October and 2014 January (see Table 1, JD 2,456,595–2,456,668), $\sigma_{\text{pos}} \approx 80$ mas.
5. GDR2 (Gaia Collaboration et al. 2018), $E_p = 2015.5$ (JD 2,457,206), $\sigma_{\text{pos}} \approx 0.03$ mas.

In Section 5.4, we also evaluate various indicators that could hint at the existence of hitherto-overlooked companions. All 31 target stars with VLA detection candidates have 2MASS, WISE, and Gaia astrometry, although we do not use the GDR2 positions for three of the sources because of the astrometric fit quality issues mentioned above (RUWE > 50 : HD 23524, HD 284135, and HD 293857). The first two of these are actually known close visual double stars. Nine stars also have Hipparcos (van Leeuwen 2010) astrometry, and for 21 stars there are at least Tycho2 positions available. Only one star has neither Hipparcos nor Tycho(2) astrometry (UCAC4 832–014013). Twenty target stars have known WDS companions, of which 14 are closer than $2''5$ to the primary (see Table 2 and discussion in Section 5.4). Five stars have significant ($> 3\sigma$) proper-motion anomalies (PMA) between the long-term HIP–Gaia proper-motion vector and the GDR2 measurements (PMAg2; Kervella et al. 2019). However, four of these five stars have known WDS companions with

separations $< 2''5$ (Mason et al. 2020), and the PMAg2 are consistent with being caused by the presence of these companions (Figures 12–15). The implications of these PMAg2 on the association between VLA and stellar positions are further discussed in Sections 4.3 and 5.4.

Figure 6 and the associated figure set show the astrometric charts for all 31 VLA detection candidates with the measured positions relative to the 2MASS position and the respective 1σ uncertainty ellipses. Positional uncertainties of the VLA detections are derived as described in Section 4.1. In addition to the observed positions, we also show the most recent and accurate estimate of the combined proper and parallactic motion along with the positions and uncertainties predicted by this motion for the epochs of the respective other catalog positions. If a star has a valid GDR2 solution, the motion vector and position predictions are projected backward in time from the mean GDR2 position. If a star has a Hipparcos/Tycho2 entry but no valid GDR2 astrometry, the motion vector and position predictions are projected forward in time starting from the observed Hipparcos/Tycho2 position. Of prime interest are of course the position predictions for the stars in question at the time of the respective VLA observations, which we compare in the following to the actually observed VLA detections. The position predictions for the other epochs/missions are only used to assess the consistency of the multiepoch astrometry for the respective star and to identify stars with generally troublesome astrometry, which could indicate, e.g., unresolved multiplicity (see, e.g., Dzib et al. 2021; Forbrich et al. 2021).

With the now more precise astrometry, the positional discrepancies between the 31 VLA detection candidates and the respective nearest known star are all well below $1''$. We find that the radio sources related to 19 target stars are securely associated with the target stars. Three targets have somewhat problematic astrometry, but we still consider the VLA detections very likely associated with the respective stars. In the following subsection, we discuss all those stars individually for which the astrometry or the association between VLA source and star had some issues.

4.3. Notes on Individual Targets

For two stars (TYC 5925-1547-1 and SAO 150676) that used the same VLA phase calibrator and that have the same large discrepancy of $\approx 0''7$ between predicted and observed VLA position, we conclude that the problem is most likely related to an unfortunate combination of calibrator choice and observing schedule. None of the two stars has a known close ($< 5''$) companion, but the respective calibrator J 0539-1550 was on the faint side (0.5 Jy) and about 5° away from the two targets. While this would have been acceptable under good conditions, the observations were carried out with the calibrator at an elevation of 21° and the two targets at 18° . This, together with the faintness of the calibrator, may be the reason for the large phase calibration error.

The third star with large positional discrepancy is SAO 50350, which is not a known binary (Mason et al. 2020), and for which the detections by Tycho2, 2MASS, WISE, and Gaia all align very well. The VLA detection is $0''72$ ($\approx 5.3\sigma$) offset from the Gaia-predicted optical position of the star, which has a well-behaved GDR2 astrometric solution (RUWE ≈ 1.0) and does not show a PMA. In this case we cannot say whether the VLA measurement is just an outlier with some astrometry issues not accounted for, or whether we

Table 2
Stars with 6 GHz Detections

No. ^a	Star ID (Other Name)	Date 1	$S_{6\text{GHz}}^1 \pm \delta$ ($\mu\text{Jy} \pm \mu\text{Jy}$)	Date 2	$S_{6\text{GHz}}^2 \pm \delta$ ($\mu\text{Jy} \pm \mu\text{Jy}$)	Δt (days)	S_1/S_2	Δr^b (arcsec (σ))	Binarity ^c	Remarks ^d
11	BD +17 232 A	2013-10-29	149 ± 18	2013-11-16	276 ± 32	18	1.85	0.32 (2.75)	WDS(1 ^{''} 7)	D12 (1)
26	HIP 12545 (BD +05 378)	2013-10-29	<52 ± 17	2013-11-16	102 ± 12	18	>1.96	0.11 (0.41)	...	D1
27	HIP 12635 (HD 16760 B)	2013-10-29	261 ± 69	2013-11-16	<63 ± 21	18	>4.14	0.27 (1.10)	K19	D1
33	V875 Per	2013-10-29	2394 ± 86	2013-11-16	1840 ± 250	18	1.30	0.07 (2.48)	WDS(5 ^{''} 8), RS CVn	D1
35	TYC 3301-2585-1	2013-10-30	154 ± 35	2013-11-6	392 ± 34	7	2.55	0.68 (4.74)	WDS(2 ^{''} 1)	D12 (2)
48	HD 22213 (BD -12 674)	2013-11-17	623 ± 24	2013-12-1	108 ± 20	14	5.77	0.11 (1.11)	WDS(1 ^{''} 7)	D1
51	HD 23524	2013-10-30	2059 ± 22	2013-11-6	727 ± 14	7	2.83	0.03 (0.22)	WDS(0 ^{''} 3)	D12 (2)
52	HD 24681 (BD -02 754)	2013-11-17	216 ± 15	2013-12-1	<61 ± 20	14	>3.54	0.08 (0.84)	...	D1
53	HD 285281 (V1293 Tau)	2013-10-30	<112 ± 37	2013-11-6	314 ± 80	7	>2.80	0.19 (0.76)	WDS(0 ^{''} 86)	D1
57	HD 284135 (V1299 Tau)	2013-10-30	386 ± 27	2013-11-6	254 ± 13	7	1.52	0.30 (1.98)	WDS(0 ^{''} 4)	D12 (1, 4)
74	HD 31281 (V1349 Tau)	2013-10-30	1089 ± 37	2013-11-6	2910 ± 31	7	2.67	0.07 (2.46)	WDS(4 ^{''} 4)	D1
77	BD -08 995	2013-11-17	197 ± 37	2013-12-1	206 ± 27	14	1.05	0.25 (0.66)	...	D1
79	HD 286264 (V1841 Ori)	2013-10-30	<69 ± 23	2013-11-6	222 ± 37	7	>3.22	0.05 (0.26)	...	D1
81	HD 293857 (BD -04 1063)	2013-11-17	659 ± 23	2013-12-1	369 ± 19	14	1.79	0.05 (0.51)	... ^d	D1
88	TYC 713-661-1	2013-11-17	214 ± 17	2013-12-1	<70 ± 23	14	>3.06	0.20 (2.34)	WDS(1 ^{''} 8)	D1
92	TYC 5925-1547-1 (CPD -19 878)	2013-11-17	274 ± 27	2013-12-1	57 ± 16	14	4.81	0.90 (2.26)	...	D1 (3)
93	SAO 150676 (AI Lep)	2013-11-17	1280 ± 250	2013-12-1	709 ± 203	14	1.81	0.64 (1.04)	WDS(8 ^{''} 4), RS CVn	D1 (3)
98	HD 62237 (BD -15 1991)	2013-11-25	91 ± 24	2014-01-3	168 ± 12	39	1.85	0.16 (1.66)	...	D1
101	SAO 135659	2013-11-25	4542 ± 34	2014-01-3	425 ± 21	39	10.7	0.05 (1.08)	WDS(0 ^{''} 14)	D12 (2)
106	HD 77407	2014-01-10	785 ± 12	0.09 (1.89)	WDS(1 ^{''} 7), K19	D2 (WDS 09035+3750 B)
108	HD 82159 (GS Leo)	2013-11-25	3852 ± 36	2014-01-3	918 ± 12	39	4.20	0.03 (0.74)	WDS(13 ^{''} 7), D15	D1
109	HD 82558 (LQ Hya)	2013-11-25	112 ± 76	2014-01-3	716 ± 15	39	6.39	0.07 (0.88)	...	D1
112	GJ 2079 (DK Leo)	2013-11-25	251 ± 16	2014-01-3	12784 ± 47	39	51	0.05 (0.87)	WDS(0 ^{''} 1), K19	D12 (2)
144	HD 135363 (BD +76 552)	2013-11-27	400 ± 47	2013-12-30	167 ± 39	33	2.40	0.49 (1.31)	WDS(0 ^{''} 36), K19	D12
153	HD 199143	2013-10-29	1305 ± 64	2013-11-17	531 ± 15	19	2.46	0.13 (0.62)	WDS(1 ^{''} 05), K19	D2 (HD 199143 B)
154	HD 358623 (AZ Cap)	2013-10-29	312 ± 74	2013-11-17	182 ± 21	19	1.71	0.29 (1.65)	WDS(2 ^{''} 2)	D1
155	SAO 50350 (BD +44 3670)	2013-10-29	181 ± 30	2013-11-17	<71 ± 24	19	>2.55	0.72 (5.26)	...	D1 (5)
159	GJ 4199 (LO Peg)	2013-10-29	245 ± 9	2013-11-17	454 ± 13	19	1.85	0.07 (0.97)	WDS(9 ^{''} 2)	D1
164	SAO 51891 (V383 Lac)	2013-10-29	1128 ± 22	2013-11-17	<90 ± 30	19	>12.5	0.08 (1.66)	WDS(4 ^{''} 0)	D1
165	SAO 108142 (BD +17 4799)	2013-10-29	992 ± 25	2013-11-17	1610 ± 950	19	1.62	0.21 (0.59)	...	D1
170	UCAC4 832-014013	2013-11-27	1070 ± 120	2013-12-30	932 ± 175	33	1.15	0.15 (0.96)	...	D1 (6)

Notes.
^a No. refers to Table 3, where also the coordinates and some basic stellar parameters are listed.
^b Absolute and relative positional discrepancy between VLA detection and predicted star position, given in arcseconds and (in brackets) in units of the combined 1 σ positional uncertainties.
^c Companions listed in the Washington Visual Double Star Catalog (WDS; Mason et al. 2020) with approximate projected separation given in brackets, or identified by Kervella et al. (2019, K19) via PMa. RS CVn indicates RS-Canum-Venaticorum variability, which indicates the presence of a very close (interacting) companion. D15 indicates the presence of a close companion with a 3.86-day period reported by Desidera et al. (2015). The star is also flagged with duplicity-induced variability in the Hipparcos catalog.
^d D1: detection of target star (primary in case of visual binarity); D2: detection of (visual) companion to target primary; D12: VLA source centered in between two binary components.
^e Large GDR2 astrometric excess noise (7.6 mas) and RUWE \approx 59 could hint at a yet-unknown companion.
^f VLA source centered closer to primary.
^g VLA source centered closer to secondary.
^h Bad calibrator (J0539-1550).
ⁱ No valid GDR2 astrometry, HIP pm probably affected by secondary.
^j VLA source center off by 5.3 σ , but star still within beam. Hint at unknown secondary?
^k UCAC4 832-014013 was not an original target star but was detected in the pointing on HD 135363.

8

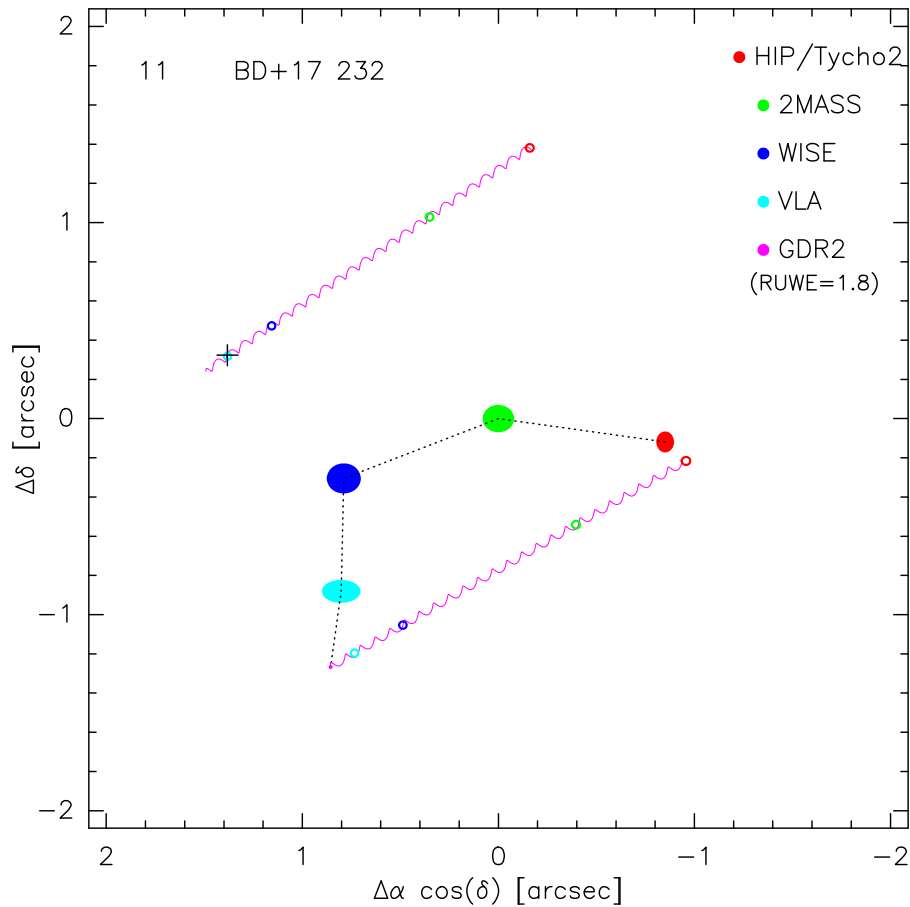


Figure 6. Astrometric chart for BD +17 232. The number in the upper left corner relates to the target number in Tables 2 and 3. Measured positions (relative to the 2MASS) and 1σ uncertainties are drawn as filled ellipses, with the color-coding for the respective missions/catalogs indicated in the upper right corner. Straight dotted lines connect the observed positions just to guide the eye. The lower wiggled line shows the combined proper-motion and parallax prediction, starting at the GDR2 2015.5 position and projected backward in time. Open ellipses show the position and uncertainty prediction from that starting point for the respective observing epochs. The black plus sign shows the position of the WDS companion BD +17 232 B (Mason et al. 2020) at the epoch of the VLA observations, i.e., relative to the center of the light-blue open ellipse marking the predicted position of the primary. The upper wiggled line and open ellipses show the proper-motion/parallax and position prediction for the secondary, which was also detected by GDR2.

(The complete figure set (31 images) is available.)

have actually detected a hitherto-unknown companion or an unrelated background source (but see discussion in Section 4.1).

For two sources, the radio emission is clearly associated with the known secondary components, and no emission is detected from the respective primaries. HD 77407 has a visual secondary at $1''.8$, which is a M3–6V physical companion to the G0V primary and was also detected by Gaia with its own astrometric solution. Our VLA detection is clearly associated with this secondary, and no radio emission is detected from the primary. The primary exhibits a large PMA (PMA_{G2} = 24.5σ). Figure 11 shows that this visual companion is compatible with having caused this PMA. The other star, HD 199143, has an about 3 mag (*V*) fainter visual secondary located at $1''.1$ northwest of the primary, which is not detected by Gaia. Our VLA detection is clearly associated with this visual secondary, and no radio emission was detected from the primary. The primary also exhibits a significant (24σ) PMA_{G2} (Kervella et al. 2019). Figure 12 shows that this visual companion is compatible with having caused this PMA.

For two sources with known visual companions at $1''.7$ and $2''.1$, the VLA detection is located in between the two binary

components, and the data do not allow us to decide from which component the radio emission arises or whether possibly both stars contribute. TYC 3301-2585-1 has an approximately equally bright (at *V* band) companion at an angular separation of $2''.1$ (**ES 1217 AB). While both components are detected separately by GDR2 (with “good” astrometric solutions), only the primary has a Tycho2 entry, and both 2MASS and WISE obviously did not resolve the source and list a position in between the two components. The VLA detection is also located in between the two components, albeit closer to the secondary. It is thus possible that the radio emission arises from both components but is not resolved by the $>2''$ VLA beam. BD +17 232 has an approximately equally bright (*V*-band) companion at $\sim 1''.7$ projected separation (WDS J01377 +1836 B). The primary is well detected by both Tycho2 and GDR2 (see Figure 6), although with moderate excess noise/RUWE for the GDR2 solution, such that the predicted position at the time of the VLA observations may have a larger (systematic) uncertainty than formally adopted. 2MASS and WISE obviously did not resolve the source and list a position in between the two components. The VLA position is also located in between the two stars, albeit only 2.8σ away from the

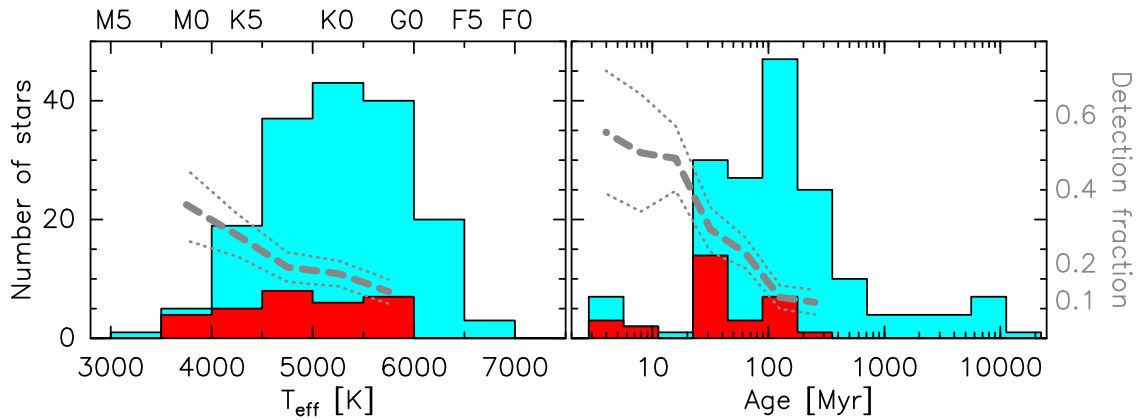


Figure 7. Distribution of stellar effective temperatures (corresponding spectral types for main-sequence stars indicated on top) and ages for the observed (light-blue histograms) and detected (at 6 GHz) stars (red histograms; see Figure 1). Shown in gray are the detection fractions (thick dashed lines; smoothed over 3 bins) with 1σ confidence intervals (dotted lines). The scale is indicated on the right side.

primary. It is thus likely that the radio emission arises from the primary only.

For five sources with known visual companions at $0''.1$ – $0''.4$, i.e., significantly smaller than the synthesized $>2''$ VLA beam, the data also do not allow us to decide from which component the radio emission arises or whether possibly both stars contribute. Statistically, one would expect that the lower-mass (i.e., cooler) component, which is in most cases the secondary, is the more likely radio emitter (assuming coevality; see Section 5.1 and Figure 7). HD 23524 has a secondary component (WDS) of approximately equal (V) brightness at $0''.3$ south of the primary. Our astrometry indicates that the detected radio emission is centered on the secondary component, although the primary is also covered by the synthesized beam. However, GDR2 indicates a large value of RUWE (9.7) for the primary and does not list solutions for parallax and proper motion. Hipparcos resolved the system as a binary, but the proper-motion solution might still be affected by the binarity.

HD 284135 also has an approximately equally bright (V -band) companion at $\sim 0''.4$ (WDS J04057+2248 B). The primary does not have a valid Hipparcos solution but is detected by both Tycho2 and GDR2, albeit in both cases with flags that indicate bad-quality solutions, such that the astrometry may be affected by the not separately detected secondary and therefore unreliable. The VLA detection is $\approx 2.5\sigma$ from the Tycho2-predicted position of the primary along the proper-motion vector (but farther away from the secondary). SAO 135659 has a secondary component (WDS) of approximately equal (V) brightness at $0''.1$ southeast of the primary. The VLA detection is centered in between the two stars.

GJ 2079 has a secondary component of approximately equal (V -band) brightness at a projected separation of $\leq 0''.1$ (≈ 2.3 au). Bowler et al. (2015) estimate an orbital period of 4.8 yr, and Kammerer et al. (2019) report the latest relative projected separation from mid-2016 as $\rho \approx 77$ mas at P.A. $\approx 339^\circ$, but a good orbit solution is not yet known. The VLA detection is within 1σ of both components, and the positional uncertainty is comparable to the separation of the two components. The primary also exhibits a large PMAg2 of $\approx 67\sigma$, and the curvature of its motion can be clearly seen in the astrometric chart (Figure 6). Figure 13 shows that the observed PMA is compatible with this visual companion.

HD 135363 has a visual secondary at $0''.36$ southeast, which is an M2/4V physical companion to the G5V primary and was not independently detected by Gaia. The primary also has a significant (9σ) PMAg2, which could be consistent with the visual secondary (Figure 14). Although our VLA detection is centered slightly closer to the primary, the M-type secondary is the more likely radio emitter.

One more target star with 6 GHz detection, HIP 12635 (HD 16760 B), exhibits a 4σ PMAg2 (Kervella et al. 2019, Figure 15) but has no known close companion. The WDS primary, HD 16760, at a projected separation of $14''.3$, which has itself a close ($\approx 0''.27$) companion (Evans et al. 2012) and exhibits a 5.6σ PMA, is actually not physically associated with HIP 12635 since it has a significantly different parallax with good-quality solution (Table 3). No radio emission was detected from HD 16760. Hence, the PMA of HIP 12635 could hint at a hitherto-undisclosed close companion. Our VLA detection is only $0''.27$ (1.1σ) offset from the Gaia-predicted position of HIP 12635, such that we consider this a secure detection.

In summary, we have thus detected radio emission from 22 target stars or their respective primaries. For seven close binary systems, the data do not allow us to decide from which of the two components the detected radio emission arises, and for two targets, the radio emission is clearly associated with the secondary components only.

4.4. Statistical Assessment of Positional Mismatches

As discussed above and shown in Figure 4, the association of radio emission with stars emitting mostly at optical and near-IR wavelengths is not at all straightforward. Even with such detailed astrometric investigations, there are remaining positional discrepancies between the radio position and the predicted optical position of the star in question, which not only may result from measurement uncertainties (both accounted and unaccounted for) but also could indicate that the radio emission does not arise from the star itself but, e.g., from a yet-unknown companion. To investigate this, we show in Figure 8 the distribution of the relative positional discrepancies (angular separation) between the predicted and the observed VLA positions and compare it to the normal distribution for all detections that we would expect if the positional discrepancies would be related entirely to purely random and uncorrelated measurement errors. We find that the

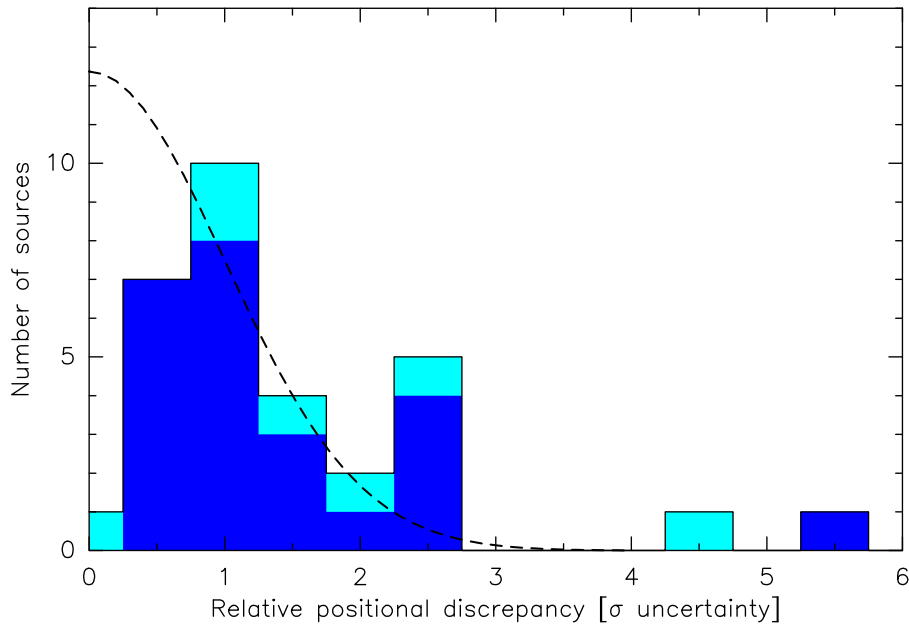


Figure 8. Number of target stars as a function of angular separation between predicted position and the nearest VLA source in units of the combined 1σ uncertainties of the two positions. The dark-blue histogram accounts for all targets in which the VLA source could be associated with one star (primary or secondary in binaries). The light-blue histogram on top indicates those sources in which two binary components are likely to contribute to the radio emission. The dashed curve shows the normal distribution for all 31 detections, i.e., the expected shape of the histogram for purely random and uncorrelated astrometric measurement errors.

distribution is roughly consistent with the expected normal distribution for random errors, but that there is a clear lack of exact matches (discrepancy $< 1\sigma$) and a slight excess of relative discrepancies between 2σ and 3σ . The figure also shows that this mismatch is unlikely to be caused entirely by the contribution of radio emission from the known but unresolved secondary components. We discuss the possible reasons in Section 5.4.

4.5. Radio Flux Variability

As described in Section 3, all but three fields were observed in two epochs separated by 7–39 days. Of the 31 stars from which radio emission was detected, 22 sources were detected in two epochs, eight sources were detected in only one epoch, and one detected object was observed only once. Flux ratios range from 1.05 up to about 11, plus one clear outlier with the strongest peak flux (12.8 mJy) and a flux ratio of 51 (GJ 2079). It is interesting to note that GJ 2079 is the closest known visual binary in our sample (projected separation ≤ 100 mas or 2.3 au) and the emission is most likely arising from both equally bright (in V band) components. GJ 2079 has the second-lowest X-ray luminosity in our radio-bright sample ($9 \times 10^{-6} L_{\odot}$; see Figure 9) but is otherwise not significantly distinguished in any property from the other radio-detected young stars. This star thus resembles the group of 13 extremely radio-variable young stars in the Orion Nebula Cluster (ONC) identified by Forbrich et al. (2017). However, since we only have two epochs of radio observations separated by 39 days, we have no further information on the timescale of this extreme variability. Lower-limit flux ratios for stars detected in only one epoch range from 2 to 12, with a median of 3.1. Ignoring the one outlier, the median flux ratio between the two epochs is ≈ 2.6 . There is no significant correlation between the variability amplitude and time lag between the two epochs, nor with stellar age or spectral type.

5. Discussion

5.1. Correlation between Radio Emission and Spectral Type

The left panel of Figure 7 shows the distribution of effective temperatures and spectral types of the stars with detected 6 GHz emission, along with that of all 170 observed stars. The latest and earliest spectral types in the observed sample are M2 ($T_{\text{eff}} \approx 3500$ K) and F4 ($T_{\text{eff}} \approx 6700$ K) (with one exception of spectral type B9.5; see Table 3). The latest and earliest spectral types with detected radio emission are M0 ($T_{\text{eff}} \approx 3800$ K) and F8 ($T_{\text{eff}} \approx 5920$ K). Figure 7 also shows that the detection fraction (smoothed over three bins) decreases from $36\% \pm 10\%$ ¹⁵ at 3800 K to $12.6\% \pm 3.3\%$ at 5900 K, i.e., by a factor of three. No star with $T_{\text{eff}} > 6000$ K was detected, although 22 such stars were observed. On the other hand, we find no significant correlation between T_{eff} (or SpT) and the strength of the 6 GHz emission if it is detected.

5.2. Correlation between Radio Emission and Age

The right panel of Figure 7 shows the distribution of ages of the stars with detected 6 GHz emission, along with that of all 170 observed stars. The youngest and oldest stars in our sample have ages of $\lesssim 5$ Myr and 12 Gyr, respectively. The youngest and oldest stars with detected radio emission have ages of $\lesssim 5$ Myr and 200 Myr, respectively, i.e., gyro-synchrotron radio emission occurs at all ages between $\lesssim 5$ and 200 Myr.¹⁶ Figure 7 also shows that the detection fraction (smoothed over three bins) decreases from $56\% \pm 20\%$ at ≤ 10 Myr to $10\% \pm 3\%$ at 100–200 Myr, i.e., by a factor of nearly six. No star older than 200 Myr was detected, although 45 such stars were observed. This suggests a significant decline of coronal gyro-synchrotron emission with age from a few to about 200 Myr and a complete

¹⁵ The 1σ confidence intervals are derived from the standard deviation of the respective binomial distributions.

¹⁶ Note that no valid age estimate could be obtained for UCAC4 832–014013.

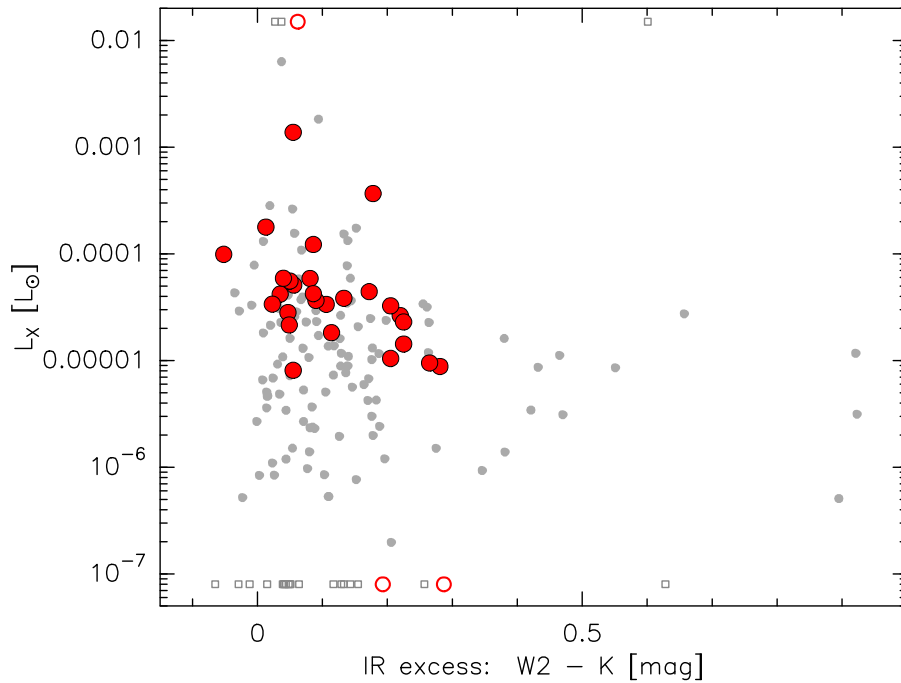


Figure 9. X-ray luminosity (2RXS absorption-corrected flux from a power-law fit; Boller et al. 2016) vs. IR excess (WISE W2(4.618 μm) minus K(2.2 μm); Skrutskie et al. 2003; Cutri et al. 2012) of observed nondetected (gray circles) and radio-detected (filled red circles) stars. Targets with X-ray nondetections or X-ray luminosities above the plot limit are shown as open squares and circles lined up at the lower and upper boundaries of the plot, respectively.

termination afterward. A general decline of stellar magnetic activity and high-energy output due to the rotational spin-down with age has been observed and modeled for the Sun and other stars by many authors (e.g., Güdel 2004; Bouvier et al. 2014; Güdel 2020). Our survey results confirm, for the first time, that strong (observable) coronal gyro-synchrotron emission indeed declines on the same timescale, or even a bit faster, as the pre-main-sequence spin-down of the stellar rotation period. On the other hand, we find no significant correlation between age and the strength of the 6 GHz emission (if it is detected) within the age range 1–200 Myr.

5.3. Correlation between Radio Emission and Infrared Excess and X-ray Activity

All but 21 out of the 170 VLA-observed stars exhibit ROSAT-detected X-ray emission. All 21 X-ray nondetected stars are older than 20 Myr. Figure 9 shows the absorption-corrected X-ray luminosity (derived from the 2RXS flux obtained from a power-law fit; Boller et al. 2016) versus IR excess (WISE W2/4.618 μm minus K/2.2 μm ; Skrutskie et al. 2003; Cutri et al. 2012) of the stars with detected 6 GHz emission, along with that of all 170 observed stars. All but three of the radio-detected stars have X-ray luminosities between $8 \times 10^{-6} L_{\odot}$ and $2 \times 10^{-3} L_{\odot}$. Only one star (HD 31281, <5 Myr) has an X-ray luminosity that is 5 orders of magnitude higher than that of the other radio-bright stars, i.e., ROSAT probably caught this star (and three other radio-nondetected stars) during an X-ray superflare (Getman & Feigelson 2021). Apart from two X-ray nondetections, no star with $L_X < 8 \times 10^{-6} L_{\odot}$ was detected at 6 GHz, although more than 70 such stars were observed. The only two radio-bright stars without an X-ray counterpart are HD 217014 and HD 358623.

Figure 9 also shows that, due to their youth and the likely existence of debris disks, nearly all of our target stars have

4.6–2.2 μm excesses of >0 mag but <1 mag. Yet only 2 out of the 31 radio-bright stars have significant debris disk excess at longer wavelengths, albeit with fractional disk luminosities $\leq 10^{-4}$ (see Figure 6 in Launhardt et al. 2020). Nevertheless, the corresponding color excess of main-sequence stars without debris disks would be very close to zero. It is also evident that all radio-bright sources have relatively small 4.6–2.2 μm excesses of $<0 \dots 0.4$ mag, and no star with IR excess >0.4 mag was detected at 6 GHz, although the number of such stars is small (13). The stars with larger IR excess have ages of 8–170 Myr, i.e., they are all in the young age range where the radio detection rate is relatively high as compared to older stars (Section 5.2 and Figure 7). Since, with a mean detection rate of $\sim 30\%$ in this younger age range, we should have detected about 3–4 out of the 13 stars observed, it is likely that the nondetection of stars with large IR excess is primarily related to the mass of the disks and not to the age. We thus conclude that future searches for stars with strong gyro-synchrotron radio emission, e.g., for identifying suitable targets for VLBA astrometry, could boost their efficiency by preselecting stars with $L_X > 5 \times 10^{-6} L_{\odot}$ and IR excess W2–K < 0.5 mag.

Figure 10 shows the relation between the 6 GHz radio luminosity (maximum of the two epochs) of observed and radio-detected stars and their respective X-ray luminosity. Most of the radio-detected stars have X-ray luminosities between 3×10^{21} and 2×10^{23} W (one outlier with 5.5×10^{23} W). While the lower boundary might be related to ROSAT’s detection limit, the upper boundary might not be significant owing to low number statistics. Most of our radio-detected stars thus roughly follow the “Güdel–Benz” relation (Güdel & Benz 1993) between “quiescent” (i.e., not accounting for flares) X-ray and radio luminosity for magnetically active stars. The few sources to the lower right of the relation might have been caught during a radio flare.

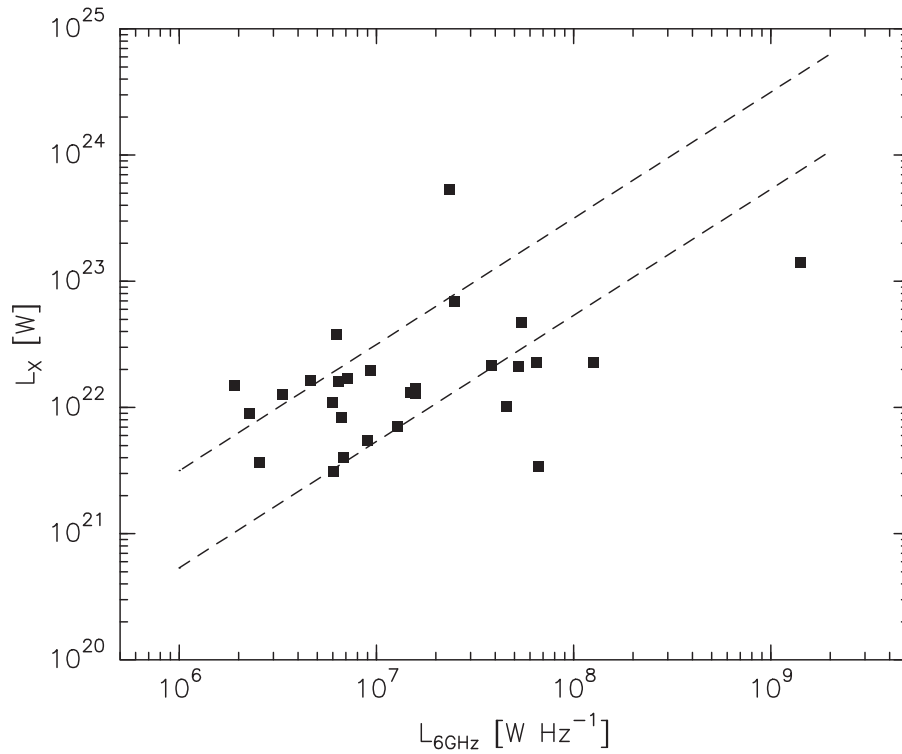


Figure 10. X-ray luminosity vs. 6 GHz radio luminosity (max of the two epochs) of observed and radio-detected stars. Dashed lines show the empirical Güdel & Benz (1993) relation between “quiescent” (i.e., not accounting for flares) X-ray and radio luminosity for different types of magnetically active stars (see Benz & Güdel 1994).

5.4. Correlation between Radio Emission and Binarity

To verify whether and to what degree binarity is related to the occurrence of gyro-synchrotron emission, we evaluate for all detection candidates the ninth catalog of spectroscopic binary orbits (SB9; Pourbaix et al. 2004) and the Washington Visual Double Star Catalog (WDS; Mason et al. 2020) and obtained the individual measurements where necessary to determine the positional offset of the components at the time of the VLA observations. Although these two catalogs are by far not complete, they provide the most complete binarity database we have available and the only useful means of comparison with binarity fractions of other surveys. In addition, we check the NASA Exoplanet Archive for known planetary companions to our radio-bright target stars, but we find none. We also look for PMaG2 (Kervella et al. 2019), which could be indicative of the presence of a perturbing secondary object but would also lead to a wrong prediction of the star position at the time of the VLA observations. In addition, we search the literature for reported companion detections. For the GDR2 astrometry, we also evaluate the renormalized “unit weight error” (RUWE; Lindegren et al. 2018), which should be close to 1.0 for well-behaved solutions of single stars. Excessively large values may indicate that not every Gaia observation was consistent with the single-star model.

We find that 20 out of the 31 radio-bright stars identified in our sample (65%) have known companions of some type, of which 14 (45% \pm 10%) have at least one component located within $2''.5$ of the primary. Two more stars (V875 Per and AI Lep) are supposed to have close (interacting) companions revealed by their photometric variability (Section 5.5), which are not directly detected. One more star without a known close companion exhibits a significant PMA (HIP 12635), which

could hint at the presence of a yet-unknown close companion. One other star (HD 293857) exhibits a large GDR2 astrometric excess noise (7.6 mas) and $\text{RUWE} \approx 59$, which could also hint at a yet-unknown companion. These indirect detections would increase the close companion fraction to $58\% \pm 10\%$ (18 stars). The Gould Belt Distances Survey (GOBELINS; Ortiz-León et al. 2017a, 2017b; Kounkel et al. 2017) reported 59 out of 156 radio-bright stars to have WDS companions at separations $\leq 2''.5$, which corresponds to a close binary fraction of 38% and is consistent with the close binary fraction based on WDS companions in our sample.

The statistical lack of exact astrometric matches between VLA detections and star positions and the excess of 2σ – 3σ positional discrepancies revealed in Section 4.2 (Figure 8) are unlikely to be caused by companion-related proper-motion uncertainties since the GDR2 positions are derived within only about 1.5 yr from the VLA observations and the mean proper motion of our targets is only about 100 mas yr^{-1} . This statistical anomaly could therefore hint at the presence of additional still-unknown close companions and thus an even higher close companion fraction. This suspicion is supported by the findings of Forbrich et al. (2021) and Dzib et al. (2021), who carried out a VLBA survey for nonthermal emission toward 556 compact radio sources previously identified in a deep VLA survey of the ONC (Forbrich et al. 2016, 2017), of which they detected 123 sources with the VLBA. Of the 34 VLBA radio sources that are associated with GDR2-listed stars within $0''.2$, 23 sources (68%) are well separated ($>4 \text{ mas}$) from the associated GDR2 position and are likely close companions of the Gaia-detected optical stars.

The WDS was also probed for the 139 radio-quiet stars in our sample, for which we find 34 stars (24% \pm 4%) to have known companions within $2''.5$ listed, i.e., the close binary

fraction of radio-bright stars is at least twice as high as that of radio-quiet stars. This significant difference in the close binary fraction between radio-loud and radio-quiet stars further suggests that binarity and gyro-synchrotron emission are closely related.

We can now use these close binary fractions to correct our star system radio detection rate of $18\% \pm 3\%$ (Section 4.1) and derive a star detection rate. Assuming for simplicity close binary fractions of $25\% \pm 5\%$ for the 139 radio-quiet systems in our sample and $50\% \pm 10\%$ for the 31 radio-detected systems, and assuming further that we have no triple systems and that only one star per system is emitting at radio wavelengths, we derive a star detection rate of 31 out of 221 stars, i.e., $14\% \pm 2\%$.

5.5. Correlation between Radio Emission and Other Activity

A total of 19 out of 31 stars (61%) detected at 6 GHz are listed as photometrically variable in SIMBAD and/or the Hipparcos and Tycho catalogs (ESA 1997). Ten of these are classified as rotationally variable owing to starspots (mostly BY Dra-type variability). Two stars are RS-Canum-Venaticorum variables (V875 Per and SAO 150676), which indicates the presence of a very close (interacting) companion in addition to the wide visual companions listed in the WDS (Mason et al. 2020). Two stars are flagged by Hipparcos to show duplicity-induced variability (HIP 12635 and HD 82159). Both stars have reported close companions (see Table 2). Four more stars are listed as irregular or not further classified variables. One star (HD 286264) is listed as a classical Cepheid, i.e., with variability caused by radial pulsations. Without having done this same assessment for the 139 radio-nondetected stars for comparison, this large fraction of documented photometric variability caused by both magnetic activity and close companions is consistent with the notion that nonthermal radio emission scales with various other indicators of variability.

6. Summary and Conclusions

We have carried out a VLA 6 GHz continuum survey for coronal radio emission from young low-mass stars in the immediate solar neighborhood at distances between 8 and 130 pc, i.e., inside the Local Bubble and the Gould Belt. In total, we have observed fields with FOV 7.5 around 170 stars with spectral types ranging from F4 to M2 and with ages ranging from $\lesssim 5$ Myr to 12 Gyr (median 149 Myr). To ensure that we also obtain a measure of the long-term flux variability, each field was observed twice, with the two observations separated by 7–39 days. One short extra session with three stars could be scheduled only once. Thus, we observed 167 stars twice, and three more stars could be observed only once. The mean synthesized FWHM beamwidth (angular resolution) of the observations was $\approx 2''$ (major axis). We achieve a mean 3σ point-source detection limit of $\approx 45 \mu\text{Jy}$. Typical (median) positional uncertainties of the centroids of detected radio sources are $0''.14$ in R.A. and $0''.19$ in decl., derived from image plane fitting. The typical uncertainty of the estimated radio flux densities is 12%.

Our survey is thus complementary to the Gould Belt VLA survey (Loinard et al. 2011; Dzib et al. 2013; Kounkel et al. 2014; Dzib et al. 2015; Ortiz-León et al. 2015; Pech et al. 2016), the hitherto-largest survey for radio continuum emission from young stars. Our targets are all located inside the Local

Bubble and the Gould Belt and are thus significantly closer to the Sun. Second, our survey covers stars with ages ranging from $\lesssim 5$ Myr to 12 Gyr, while the oldest stars associated with the Gould Belt are only about 30 Myr old (e.g., Stothers & Frogel 1974).

In total, we have identified ≥ 626 radio sources with fluxes above the 3σ threshold and with peak fluxes between $50 \mu\text{Jy}$ and 900 mJy (median $500 \mu\text{Jy}$). Of these, 31 radio sources with fluxes between $68 \mu\text{Jy}$ and 13 mJy (median 266 mJy) are clearly associated with 31 out of our 170 target stars. The positional uncertainties of these radio sources are smaller than those of the entire sample (because they are brighter than the majority of the background sources) and amount to 70–80 mas (median). None of the remaining 139 target stars were found to exhibit detectable radio emission at the time of the observations. We also find that, apart from UCAC4 832–014013, none of the remaining ≥ 595 VLA radio sources are associated with another known star, and we conclude that these radio sources are likely related to background sources (radio galaxies, quasars).

With 31 out of 170 surveyed stars (not counting companions) exhibiting 6 GHz radio emission above the mean 3σ detection limit of $\approx 45 \mu\text{Jy}$, the overall system detection rate amounts to $18\% \pm 3\%$. Of these, 22 sources (71%) were detected in both epochs, eight sources were detected in only one out of two epochs, and one detected object was observed only once. Fluxes are varying for nearly all sources between the two epochs, with flux ratios ranging from 1.05 up to >12.5 , a median flux ratio of ≈ 2.6 , and one outlier with a flux ratio of 50. There is no significant correlation between the variability amplitude and the time lag between the two epochs, nor with stellar age or spectral type. Our system detection rate thus compares well with the system detection rate in the Ophiuchus complex ($\approx 16\%$; Dzib et al. 2013) but is significantly lower than in Taurus ($\approx 35\%$; Dzib et al. 2015). Our binarity-corrected star detection rate is slightly lower and amounts to $14\% \pm 2\%$, assuming that the radio emission in binary systems arises from only one of the two stars.

We find a significant decline of the detection rate with age by a factor of five to six from $56\% \pm 20\%$ for stars with ages ≤ 10 Myr to $10\% \pm 3\%$ for stars with ages 100–200 Myr. No star older than 200 Myr was detected, although 45 such stars were observed. The latest and earliest spectral types with detected radio emission in our sample are M0 and F8. We also find that the radio detection rate significantly declines with T_{eff} by a factor of 2.5 ± 1.4 from $36\% \pm 10\%$ for stars with $T_{\text{eff}} < 4000 \text{ K}$ (SpT later than K8) to $12.6\% \pm 3\%$ for stars with $T_{\text{eff}} > 5000 \text{ K}$ (SpT earlier than K2). No star with $T_{\text{eff}} > 6000 \text{ K}$ was detected, although 22 such stars were observed.

We find that the fraction of known visual binarity among the radio-bright stars is at least twice as high as that of radio-quiet stars ($50\% \pm 10\%$ vs. $24\% \pm 4\%$). Both some indirect binarity indicators like certain types of variability or PMa and a statistical lack of exact positional matches between radio sources and star positions, together with an excess of 2σ – 3σ positional discrepancies (corresponding to projected separations of 10–20 au), suggest that the actual binary fraction among radio-bright stars could be significantly higher ($>60\%$). We may thus have detected radio emission from still-unknown companions in at least a few cases, although none of our radio-bright stars have a known planetary companion. The significant difference in the close binary fraction between radio-loud and

radio-quiet stars confirms that binarity and gyro-synchrotron emission are closely related, i.e., that gyro-synchrotron emission is triggered by the presence of a close companion.

All but three of the radio-detected stars have X-ray luminosities between $8 \times 10^{-6} L_{\odot}$ and $2 \times 10^{-3} L_{\odot}$. No star with $L_X < 8 \times 10^{-6} L_{\odot}$ was detected at 6 GHz, although more than 70 such stars were observed. Due to their youth and the likely existence of debris disks, our target stars have 4.6–2.2 μm IR excesses of 0–1 mag. However, the radio-bright stars have relatively small 4.6–2.2 μm excesses of 0–0.4 mag, and no star with IR excess >0.4 mag is detected at 6 GHz. We conclude that the nondetection of stars with large IR excess is primarily related to the mass of the disks, which could in turn be related to the larger fraction of close binarity as compared to radio-quiet stars. Our findings suggest that the efficiency of future searches for stars with detectable gyro-synchrotron emission can be greatly enhanced when the target list is restricted to stars with spectral types later than G0 ($T_{\text{eff}} < 6000$ K), ages $< 200\text{--}300$ Myr, X-ray luminosity $L_X > 5 \times 10^{-6} L_{\odot}$, and only moderate 4.6–2.2 μm IR excesses of $\lesssim 0.5$ mag.

The radio-bright nearby young stars identified here provide an interesting sample for future astrometric studies using VLBI arrays aimed at searching for hitherto-unknown tight binary components or even exoplanets. The promising potential of such an approach, for both identifying hitherto-unknown companions and obtaining high-precision astrometry, has been demonstrated recently by Forbrich et al. (2021) and Dzib et al. (2021). However, these studies also showed that, due to the strongly variable nature of the coronal gyro-synchrotron emission, not all VLA-detected sources might be detectable later with the VLBA.

We thank Neil Zimmerman for helping with the initial target list compilation, Ingo Stolz for setting up and maintaining our target star database, and Grant Kennedy for providing his stellar atmosphere and blackbody fitting toolbox. The National Radio Astronomy Observatory is a facility of the National Science Foundation operated under cooperative agreement by Associated Universities, Inc. This research has made use of the SIMBAD database and the VizieR catalog access tool, both

operated at CDS, Strasbourg, France. The original description of the VizieR service was published in A&AS 143, 23. This publication makes use of data products from the Two Micron All Sky Survey, which is a joint project of the University of Massachusetts and the Infrared Processing and Analysis Center/California Institute of Technology, funded by the National Aeronautics and Space Administration and the National Science Foundation. This work has made use of data from the European Space Agency (ESA) mission Gaia (<https://www.cosmos.esa.int/gaia>), processed by the Gaia Data Processing and Analysis Consortium (DPAC; <https://www.cosmos.esa.int/web/gaia/dpac/consortium>). Funding for the DPAC has been provided by national institutions, in particular the institutions participating in the Gaia Multilateral Agreement. This research has made use of the Washington Double Star Catalog maintained at the U.S. Naval Observatory. This research has made use of the NASA Exoplanet Archive, which is operated by the California Institute of Technology, under contract with the National Aeronautics and Space Administration under the Exoplanet Exploration Program. L.L. acknowledges the support of CONACyT-AEM grant 275201, CONACyT-CF grant 263356, and UNAM DGAPA/PAPIIT grants IN112417 and IN112820. T.H. acknowledges support from the European Research Council under the Horizon 2020 Framework Program via the ERC Advanced Grant Origins 83 24 28. S.R. acknowledges support through the DFG Research Unit FOR2544 “Blue Planets around Red Stars,” program RE 2694/8-1. We thank the anonymous referee for comments and suggestions that have helped to improve the clarity of the paper.

Facilities: VLA, Exoplanet Archive.

Appendix A List of Observed Stars

Table 3 shows the complete list of observed stars, including their basic parameters of distance, spectral type, and age, as well as the respective observing session and pointing numbers.

Table 3
List of Observed Stars

No.	Star ID ^a	R.A.(J2000)	Decl.(J2000)	Dist. ^b (pc)	SpT	Age (Myr)	Assoc. ^c	S ^d	P ^e	Age Reference
1	HD 166	00:06:36.785	+29:01:17.40	13.8	K0V	250	field	1	2	1
2	HD 377	00:08:25.746	+06:37:00.49	38.5	G2V	220	field	1	15	1
3	HD 691	00:11:22.438	+30:26:58.47	34.3	K0V	339	field	1	1	2
4	HD 984	00:14:10.254	-07:11:56.84	45.9	F5V	444	field	1	16	2
5	HD 1405	00:18:20.890	+30:57:22.23	28.3	K2V	149	AB Dor	1	3	3
6	HD 4277	00:45:50.889	+54:58:40.20	57.6	F8V	149	AB Dor	7	23	3
7	HD 5996	01:02:57.223	+69:13:37.42	26.4	G5V	914	field	7	24	2
8	HD 6569	01:06:26.153	-14:17:47.11	45.4	K1V	149	AB Dor	1	17	3
9	HIP 6276	01:20:32.268	-11:28:03.74	35.3	G9V	149	AB Dor	1	18	3
10	HD 10008	01:37:35.466	-06:45:37.53	24.0	G5V	24	beta Pic	1	19	3
11	BD +17 232	01:37:39.410	+18:35:33.26	52.1	K3VE	10	field	1	10	4
12	HD 10195	01:42:06.406	+69:05:09.60	45.4	F5	682	field	7	25	1
13	HD 10780	01:47:44.835	+63:51:09.00	10.0	K0V	200	CARN	7	26	5
14	BD -16 351	02:01:35.610	-16:10:00.68	88.2	K1V(e)	42	field (COL)	1	20	6, 3
15	HD 13357	02:10:52.079	+13:40:59.79	42.9	G5IV	2940	field	1	11	2
16	HD 13482	02 12:15.410	+23:57:29.53	32.1	K1V	149	AB Dor	1	12	3
17	HD 14082 B	02:17:24.734	+28:44:30.33	39.7	G2V	24	beta Pic	1	13b	3
18	HD 14082 A	02:17:25.287	+28:44:42.16	39.7	F5V	24	beta Pic	1	13a	3
19	HD 14062	02:18:24.478	+54:16:45.33	406	K0	24	beta Pic	2	1	2
20	HD 15013	02:26:09.591	+34:28:10.03	44.4	G5V	112	field (PLE)	1	5	7, 21, 22
21	HD 15115	02:26:16.245	+06:17:33.19	49.0	F4IV	45	THA	1	24	3
22	BD +30 397 B	02:27:28.048	+30:58:40.53	41.1 ^f	M2Ve	24	beta Pic	1	4b	3
23	HIP 11437	02:27:29.254	+30:58:24.61	41.1	K7V	24	beta Pic	1	4a	3
24	HD 15526	02:29:35.032	-12:24:08.63	116	G5/6V	60	field	1	25	8
25	HD 16765	02:41:13.997	-00:41:44.38	22.2	F7IV	611	field	1	21	2
26	HIP 12545	02:41:25.888	+05:59:18.42	44.4	K6Ve	10	field	1	22	8
27	HIP 12635	02:42:20.949	+38:37:21.16	49.3	K2V	149	AB Dor	1	6b	3
28	HD 16760	02:42:21.311	+38:37:07.23	69.5	G2V	6420	field	1	6a	2
29	HD 17250	02:46:14.609	+05:35:33.33	57.1	F8	45	THA	1	23	3
30	HD 17190	02:46:15.208	+25:38:59.65	25.3	K2IV	6710	field	1	9	2
31	HD 17332 A	02:47:27.227	+19:22:20.82	33.1	G6V	149	AB Dor	2	11a	3
32	HD 17332 B	02:47:27.421	+19:22:18.56	33.2	G1V	149	AB Dor	2	11b	3
33	V875 Per	02:52:17.597	+36:16:48.19	250	K2IV	63	field	1	7	9
34	HD 17925	02:52:32.128	-12:46:10.97	10.4	K1V	200	field	1	26	1
35a	TYC 3301-2585-1	02:55:43.821	+47:46:46.46	50.0	K5Ve	42	COL ⁱ	2	2	3
35b	WDS 02557+4746 B	02:55:43.621	+47:46:46.47 ^g	50.1	...	42 ^h	COL	2	2	3
36	TYC 1794-419-1	02:58:28.763	+29:47:53.78	187	K0IV	100	field	1	8	9
37	HD 18803	03:02:26.026	+26:36:33.26	21.2	G8V	6540	field	2	12	2
38	BD +29 525	03:07:59.210	+30:20:26.07	90.0	G5IV	160	field	2	5	9
39	HD 19668	03:09:42.288	-09:34:46.58	38.7	G0V	149	AB Dor	1	27	3
40	TYC 654-1274-1 ^j	03:10:12.545	+14:36:03.00	110	G6V	63	field	2	14	9
41	HIP 14809	03:11:13.841	+22:24:57.11	50.7	G5V	149	AB Dor	2	13	3
42	HD 19994	03:12:46.437	-01:11:45.96	22.5	F8V	45	ARG	3	1	10
43	HD 20385	03:16:40.671	-03:31:48.92	48.8	F6V	45	THA	3	2	3
44	HD 20367	03:17:40.045	+31:07:37.36	26.1	G0	613	field	2	6	2
45	BD -19 660	03:20:50.711	-19:16:08.76	44.1	K7V	42	COL	3	6	3
46	HD 21845	03:33:13.491	+46:15:26.53	36.4	G5V	149	AB Dor	2	3a	3
47	HD 21845 B	03:33:14.04	+46:15:19.4	36.4	M0Ve	149	AB Dor	2	3b	3
48	HD 22213	03:34:16.357	-12:04:07.27	51.5	G7V	45	THA	3	7	3
49	HD 22179	03:35:29.904	+31:13:37.44	70.4	G5IV	30	field	2	7	2
50	BD +27 555	03:44:24.243	+28:12:23.19	65.3	G7V	63	field	2	8	9
51a	HD 23524	03:48:23.113	+52:02:15.01	51.7 ^g	G8	42	COL	2	4	3
51b	HD 23524 B	03:48:23.113	+52:02:14.79 ^k	51.7 ⁿ	K1V	42 ^h	COL	2	4	3
52	HD 24681	03:55:20.406	-01:43:45.21	56.1	G8V	149	AB Dor	3	3	3
53	HD 285281	04:00:31.069	+19:35:20.85	135	K1	1.5	TAU	2	15	9
54	BD -15 705	04:02:16.487	-15:21:29.82	54.3	K3/4	45	THA	3	8	3
55	HD 25457	04:02:36.745	-00:16:08.12	18.8	F6V	149	AB Dor	3	4	3
56	HD 25680	04:05:20.258	+22:00:32.05	16.9	G5V	45	ARG	2	17	10
57	HD 284135	04:05:40.579	+22:48:12.03	80 ^l	G3V:	1.5	TAU	2	16	11
58	HD 25953	04:06:41.534	+01:41:02.08	57.0	F5	149	AB Dor	3	5	3
59	HD 281691	04:09:09.740	+29:01:30.34	110	G8III	16	field	2	19	2
60	HD 25665	04:09:35.039	+69:32:29.01	18.8	G5V	149	AB Dor ^j	2	18	3
61	HD 26182	04:10:04.692	+36:39:12.25	107	G0V	63	field	2	9	9
62	HD 284266	04:15:22.917	+20:44:16.90	120	K0V:	1.5	TAU	2	18	11
63	HD 285751	04:23:41.321	+15:37:54.87	104	K2V:	1.5	TAU	2	20	11
64	HD 279788	04:26:37.399	+38:45:02.28	170	G5V	40	field	2	10	9
65	HD 28344	04:28:48.297	+17:17:07.67	46.7	G2V	750	HYA	2	21	12
66	HD 285840	04:32:42.433	+18:55:10.23	90.5	K1V:	1.5	TAU ^j	2	22	11
67	BD -12 943	04:36:47.102	-12:09:20.67	68.9	K0V	45	THA	3	9	3
68	TYC 91-82-1	04:37:51.493	+05:03:08.62	93.9	K2V	150	field (AB Dor)	3	26	6, 3
69	HD 29623	04:39:23.768	-12:31:47.91	68.8	G0V	90	field	3	11	8

Table 3
(Continued)

No.	Star ID ^a	R.A.(J2000)	Decl.(J2000)	Dist. ^b (pc)	SpT	Age (Myr)	Assoc. ^c	S ^d	P ^e	Age Reference
70	HD 29697	04:41:18.856	+20:54:05.45	13.2	K3V	257	field	2	23	2
71	HD 29883	04:43:35.436	+27:41:14.64	21.9	K5V	112	field (PLE)	2	24	7, 21, 22
72	HD 30495	04:47:36.291	-16:56:04.04	13.2	G1.5V	45	ARG	3	11	10
73	HD 30652	04:49:50.411	+06:57:40.59	8.0	F6V	1570	field	3	27	2
74	HD 31281	04:55:09.622	+18:26:31.13	122	G1V:	1.5	TAU	2	25	11
75	HD 286179	04:57:00.645	+15:17:53.14	124	G3V:	1.5	TAU	2	26	11
76	HD 31652	04:57:22.323	-09:07:59.63	91.1	G8V	150	field (AB Dor)	3	21	6, 3
77	BD -08 995	04:58:48.534	-08:43:39.79	87.3	K0V	42	field (COL)	3	20	6, 3
78	BD -19 1062	04:59:32.027	-19:17:41.66	66.9	K3V(e)	45	field (THA)	3	12	6, 3
79	HD 286264	05:00:49.287	+15:27:00.71	53.4	K2IV	24	beta Pic	2	27	3
80	HD 32981	05:06:27.688	-15:49:30.38	85.1	F8V	149	AB Dor ⁱ	3	13	3
81	HD 293857	05:11:09.676	-04:10:54.37	78 ^m	G8V	24	beta Pic	3	22	3
82	BD -09 1108	05:15:36.518	-09:30:51.55	82.5	G5V	45	field (THA)	3	23	6, 3
83	HD 35112	05:22:37.491	+02:36:11.49	19.8	G5V	45	field (IC 2391)	3	28	13
84	BD -08 1115	05:24:37.249	-08:42:01.76	158	G7V(e)	42	field (COL)	3	24	6, 3
85	HD 35850	05:27:04.763	-11:54:03.48	26.9	F8V(n)k:	24	beta Pic	3	14	3
86	BD -19 1194	05:30:19.075	-19:16:31.85	113	G5V	42	field (COL)	3	16	6, 3
87	HD 36869	05:34:09.162	-15:17:03.18	57.9	G3V	42	COL	3	15	3
88	TYC 713-661-1	05:36:50.055	+13:37:56.11	57.0	K0V	149	AB Dor	3	30	3
89	TYC 119-1242-1	05:37:45.335	+02:30:57.52	68.2	K4V	42	COL ^j	3	29a	3
90	TYC 119-497-1	05:37:46.501	+02:31:26.44	68.4	K5V	42	field (COL)	3	29b	6, 3
91	TYC 4779-394-1	05:38:56.636	-06:24:40.97	124	G8V	150	field (AB Dor)	3	25	6, 3
92	TYC 5925-1547-1	05:39:23.169	-19:33:29.45	77.9	K1V	150	field (AB Dor)	3	17	6, 3
93	SAO 150676	05:40:20.732	-19:40:10.99	73.0	G2V	42	COL	3	18	3
94	BD -13 1328	06:02:21.897	-13:55:32.59	45.2	K4V(e)	149	AB Dor	3	19	3
95	HD 48737	06:45:17.364	+12:53:44.13	18.2	F5IV	1700	field	4	1	14
96	TYC 1355-214-1	07:23:43.592	+20:24:58.66	27.8	K5Ve	149	AB Dor	4	2	3
97	GJ 281	07:39:23.039	+02:11:01.19	15.1	K7	300	field	4	3	15
98	HD 62237	07:42:26.574	-16:17:00.37	124	G5V	42	field (COL)	4	4	6, 3
99	GJ 9251 B	08:07:08.777	+07:22:58.39	43.9	K5	112	field (PLE)	4	8b	7, 21, 22
100	GJ 9251 A	08:07:09.095	+07:23:00.13	41.5	K8	112	field (PLE)	4	8a	7, 21, 22
101a	SAO 135659	08:13:50.993	-07:38:24.61	53.9	K0	42	COL	4	5	3
101b	WDS 08138-0738 B	08:13:50.998	-07:38:24.52 ^k	53.9	...	42 ^h	COL	4	5	3
102	HIP 40774	08 19 19.051	+01 20 19.91	22.4	G5V	200	CARN	4	6	1, 5
103	HD 70573	08 22 49.951	+01 51 33.55	59.3	G6V	66	field	4	7	2
104	HD 70516	08 24 15.656	+44 56 58.96	36.9	G0V	280	field	8	1	2
105	HIP 42253	08 36 55.782	+23 14 47.95	39.2	K5V	45	field (IC 2391)	4	17	7
106a	HD 77407	09 03 26.973	+37 50 24.98	30.2	G0V:	42	COL	8	3	3
106b	WDS 09035+3750 B	09 03 26.977	+37 50 26.70 ^g	33.9	M3-6V	42 ^h	COL	8	3	3
107	HD 78141	09 07 18.077	+22 52 21.57	25.3	K0	232	field	4	18	2
108	HD 82159	09 30 35.834	+10 36 06.31	35.2	G9V	150	field	4	14	16
109	HD 82558	09 32 25.568	-11 11 04.70	18.3	K0V	43	field	4	9	2
110	HD 82443	09 32 43.759	+26 59 18.70	18.1	K0V	204	field	4	19	2
111	HD 82939	09 36 04.278	+37 33 10.36	38.8	G5V	112	field (PLE)	8	3	7, 21, 22
112a	GJ 2079	10 14 19.177	+21 04 29.55	23.4	M0.7V	24	field (beta Pic)	4	15	24, 3
112b	WDS 10143+2104 B	10 14 19.180	+21 04 29.48 ^k	23.4	...	24 ^h	field (beta Pic)	4	15	17
113	HD 89449	10 19 44.167	+19 28 15.29	20.9	F6IV	3100	field	4	16	18
114	HD 90905	10 29 42.229	+01 29 28.04	31.0	G1V	350	field	4	11	1
115	HD 91901	10 36 30.792	-13 50 35.82	31.9	K2V	966	field	4	10	2
116	HD 94765	10 56 30.798	+07 23 18.51	17.3	K0V	200	field (Castor)	4	12	7
117	HD 96064	11 04 41.474	-04 13 15.92	26.2	G8V	233	field	4	13	2
118	HD 98736	11 21 49.343	+18 11 24.02	32.5	G5	8920	field	5	1	2
119	HD 99303	11 25 39.948	+20 00 07.68	31.5	G5V	112	field (PLE)	5	2	7, 21, 22
120	HD 102195	11 45 42.292	+02 49 17.33	29.4	K0V	1650	field	5	4	2
121	HD 102392	11 47 03.836	-11 49 26.58	25.9	K4.5V	5940	field	5	12	19
122	TYC 870-798-1	11 47 45.730	+12 54 03.40	61.4	K5Ve	126	field	5	3	9
123	HD 104576	12 02 39.454	-10 42 49.10	54.4	G3V	451	field	5	13	2
124	HD 104860	12 04 33.731	+66 20 11.72	45.2	F8	249	field	5	21	2
125	HD 105631	12 09 37.257	+40 15 07.40	25.1	K0V	200	CARN	5	18	5
126	HD 105963	12 11 27.754	+53 25 17.45	39.9	K0V	609	field	5	19	2
127	HD 107146	12 19 06.502	+16 32 53.86	27.5	G2V	150	field	5	5	1
128	HD 108574	12 28 04.447	+44 47 39.53	45.6	G5V	200	CARN	5	20a	5
129	HD 108575	12 28 04.800	+44 47 30.48	45.6	K V	200	CARN	5	20b	5
130	HD 108767	12 29 51.855	-16 30 55.55	26.0	K0V	128	field	5	14	2
131	HD 108944	12 31 00.736	+31 25 25.80	45.0	F9V	160	field	5	6	9
132	HD 109157	12 32 27.436	+28 05 04.64	43.8	G7V	112	field (PLE)	5	7	7, 21, 22
133	BD +60 1417	12 43 33.272	+60 00 52.66	45.0	K0	203	field	5	22	2
134	HD 111395	12 48 47.048	+24 50 24.82	17.1	G5V	1430	field	5	8	2
135	HIP 62686	12 50 41.858	+20 32 05.07	38.3 ⁿ	K5	45	field (IC 2391)	5	9	7
136	HD 111813	12 51 38.409	+25 30 31.81	38.7	K1V	45	field (IC 2391)	5	10	7
137	HD 112196	12 54 40.016	+22 06 28.56	35.2	F8V	80	field	5	11	9

Table 3
(Continued)

No.	Star ID ^a	R.A.(J2000)	Decl.(J2000)	Dist. ^b (pc)	SpT	Age (Myr)	Assoc. ^c	S ^d	P ^e	Age Reference
138	HD 113449	13 03 49.655	−05 09 42.52	20.5	K1V	187	field	4	20	2
139	HD 116956	13 25 45.533	+56 58 13.78	21.7	G9V	597	field	5	23	2
140	HD 118100	13 34 43.207	−08 20 31.34	20.5	K5Ve	353	field	5	15	2
141	HIP 67092	13 45 05.340	−04 37 13.23	29.4	K5	5200	field	5	16	19
142	HD 120352	13 48 58.192	−01 35 34.64	33.6	K0	45	field (IC 2391)	5	17	7
143	HD 121979	13 56 17.761	+66 56 41.02	46.0	K0V	45	field (IC 2391)	5	24	7
144	HD 135363	15 07 56.262	+76 12 02.68	29.6	G5V	45	field (IC 2391)	5	25a	7
145	HD 139777	15 29 11.186	+80 26 54.97	21.8	G1.5V	12000	field	5	26	20
146	HD 139813	15 29 23.594	+80 27 00.97	21.8	G9V	235	field	5	27	2
147	TYC 486-4943-1	19 33 03.758	+03 45 39.67	70.2	K3V	150	field (AB Dor)	7	1	6, 3
148	HD 189285	19 59 24.103	−04 32 06.20	71.6	G7V	150	field (AB Dor)	7	2	6, 3
149	BD −03 4778	20 04 49.361	−02 39 20.31	66.9	K1V	150	field (AB Dor)	7	3	6, 3
150	HIP 101262	20 31 32.072	+33 46 33.14	26.9	K5	45	field (IC 2391)	7	17	7
151	HD 199058	20 54 21.083	+09 02 23.83	75.6	G5V	244	field	7	5	2
152	TYC 1090-543-1	20 54 28.006	+09 06 06.66	74.9	K4Ve	150	field (AB Dor)	7	6	23, 3
153a	HD 199143	20 55 47.674	−17 06 51.04	46.0	F7V	24	beta Pic	7	7	3
153b	HD 199143 B	20 55 47.637	−17 06 51.58 ^k	46.0	M2	24 ^h	beta Pic	7	7	3
154	HD 358623	20 56 02.738	−17 10 53.73	45.9	K6Ve	24	beta Pic	7	8	3
155	SAO 50350	21 00 47.108	+45 30 10.91	51.8	F8	200	field	7	18	2
156	HD 201919	21 13 05.271	−17 29 12.61	38.2	K6Ve	149	AB Dor	7	9	3
157	HD 202575	21 16 32.468	+09 23 37.77	16.2	K3V	457	field	7	4	2
158	HD 203030	21 18 58.219	+26 13 49.95	39.3	G8V	445	field	7	13	2
159	GJ 4199	21 31 01.713	+23 20 07.37	24.2	K5Ve	149	AB Dor	7	14	3
160	HD 206860	21 44 31.329	+14 46 18.98	18.1	G0V	400	field	7	15	2
161	HD 209458	22 03 10.772	+18 53 03.54	48.4	G0V	6850	field	7	16	2
162	HD 209779	22 06 05.336	−05 21 28.91	36.4	G0V	838	field	7	10	2
163	HD 211472	22 15 54.139	+54 40 22.40	22.0	K1V	45	ARG	7	20	10
164	SAO 51891	22 20 07.026	+49 30 11.76	34.4	K1V	37	field	7	21	2
165	SAO 108142	22 44 41.545	+17 54 18.30	49.7	K0	149	AB Dor	7	11	3
166	HD 217014	22 57 27.980	+20 46 07.79	15.5	G2.5IVa	8810	field	7	12	2
167	HD 218866	23 10 24.624	+64 31 47.58	36.1	F8	5000	field	7	22	20
168	HIP 115162	23 19 39.561	+42 15 09.83	51.3	G4	149	AB Dor	7	19	3
169	GJ 900	23 35 00.276	+01 36 19.44	20.8	K7V	200	CARN	1	14	5
170	UCAC4 832-014013^o	15 07 57.226	+76 13 59.15	29.7	M4.5V	...	field	5	25b	...

Notes.^a Stars with VLA detections are marked in boldface and listed in Table 2 with additional information.^b Distances are derived from GDR2 parallaxes unless noted otherwise. Values ≥ 100 pc are rounded to integer pc.^c Association if membership probability is $>80\%$ according to Banyan Σ (Gagné et al. 2018). Individual cases, in which membership probabilities are only 55%–75%, are marked. Association memberships adopted from other authors are listed in brackets.^d Session no. (see Table 1).^e Pointing no. in session. If multiple targets in one pointing, star at phase center is marked “a” and off-center star is marked “b.”^f GDR2 distance from HIP 11437 adopted.^g Independent GDR2 coordinates and parallax.^h Age estimate of primary adopted.ⁱ Membership probability 55%–80% according to Banyan Σ , but association and MG age widely used in the literature.^j The originally selected pointing center was star 2E 0307.4+1424 at 03:10:14.20, +14:35:47.0. However, this star is not visible on any VIS or near-IR images, and the properties that are assigned to it resemble suspiciously clearly those of the nearby visible star TYC 654-1274-1. No radio continuum emission was detected at either of the two positions.^k No independent GDR2 coordinates, WDS relative coordinates used.^l No GDR2 nor Hipparcos parallax, distance from Carpenter et al. (2009).^m No GDR2 nor Hipparcos parallax, distance from da Silva et al. (2009).ⁿ No GDR2 parallax, distance from Hipparcos (van Leeuwen 2010).^o UCAC4 832-014013 was not in our original target list but turned out to be the only nontargeted star from which we detected 6 GHz radio emission (see Section 4.1).**References.** (1) Pearce et al. 2022; (2) Stanford-Moore et al. 2020; (3) Bell et al. 2015; (4) Galicher et al. 2016; (5) Zuckerman et al. 2006; (6) da Silva et al. 2009; (7) Montes et al. 2001; (8) Weise et al. 2010; (9) Carpenter et al. 2009; (10) Zuckerman 2019; (11) Kenyon & Hartmann 1995; (12) Brandt & Huang 2015; (13) Maldonado et al. 2010; (14) David & Hillenbrand 2015; (15) Nielsen et al. 2019; (16) Desidera et al. 2015; (17) Nakajima & Morino 2012; (18) Gáspár et al. 2016; (19) Brandt et al. 2014; (20) Holmberg et al. 2009; (21) Gagné et al. 2018; (22) Dahm 2015; (23) Desidera et al. 2021; (24) Binks & Jeffries 2016.

Appendix B

Analysis of Proper-motion Anomalies

Here we analyze the the PMA of those five target stars with 6 GHz detections for which Kervella et al. (2019) found a significant ($>3\sigma$) discrepancy between the long-term (Hipparcos–Gaia) proper-motion vector and the GDR2 measurements, which could be indicative of the presence of a perturbing secondary object. In this analysis, we follow the formalism laid out by Kervella et al. (2019). Masses and their uncertainties of

the secondary components are estimated from the spectral type of the secondary (where listed in the WDS) and from the V magnitude difference, together with BT-Settl evolutionary models (Allard 2014; Baraffe et al. 2015). The current angular separations are adopted from the individual measurements obtained from the WDS (Mason et al. 2020). Figures 11–15 show the relation between a companion’s mass and its orbital radius that can explain the observed PMAg2 for HD 77407, HD 199143, GJ 2079, HD 135363, and HIP 12635, respectively.

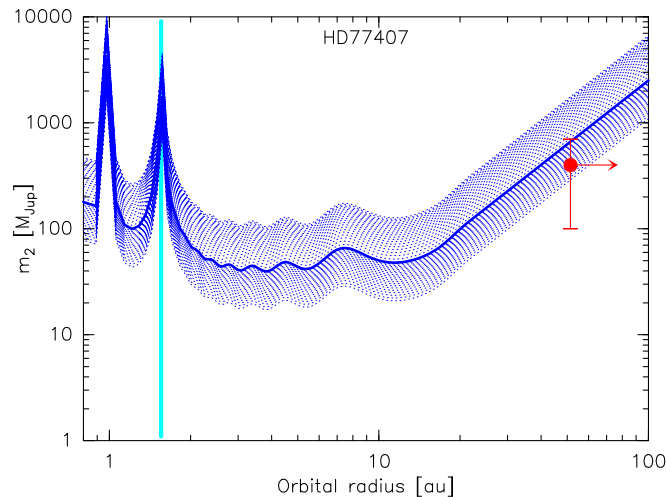


Figure 11. Analysis of PMA after Kervella et al. (2019) for HD 77407. The blue line and shaded area (1σ uncertainty domain) show the relation between a companion’s mass (in Jupiter masses) and its orbital radius (in au) that can explain the observed PMA, taking into account the GDR2 time window (668 days). The cyan vertical line marks the orbital radius, the period of which corresponds to the GDR2 time window. The red circle marks the parameters of the known visual companion WDS 09035+3750 B. The arrow indicates that the current projected separation is a lower limit to the orbital radius (assuming zero or low eccentricity).

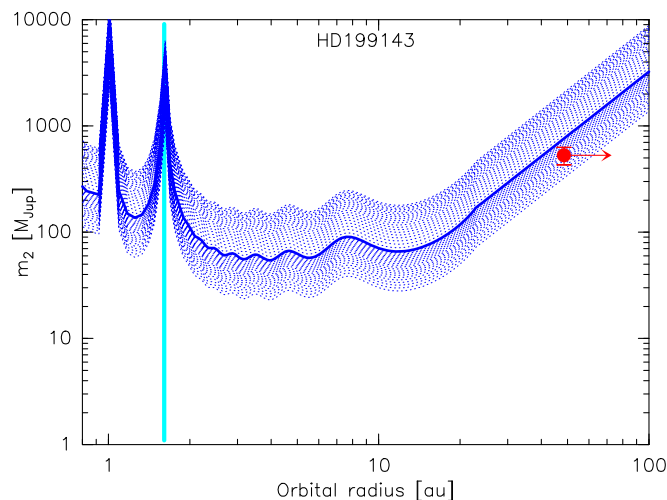


Figure 12. Same as Figure 11, but for HD 199143. The red circle marks the parameters of the known visual companion WDS 09035+3750 B.

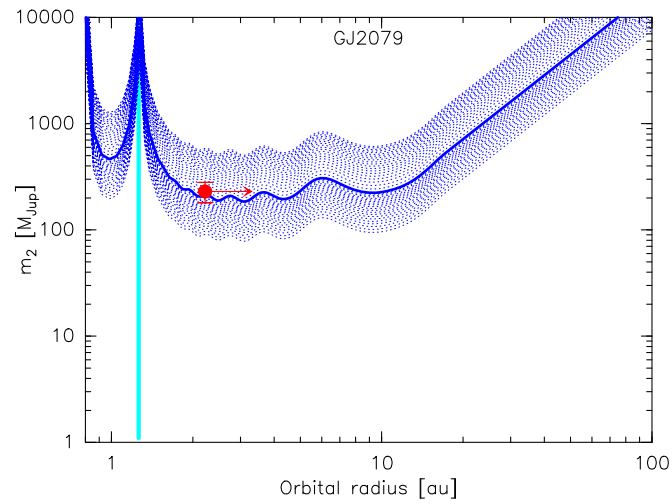


Figure 13 Same as Figure 11, but for GJ 2079. The red circle marks the parameters of the known visual companion WDS 09035+3750 B.

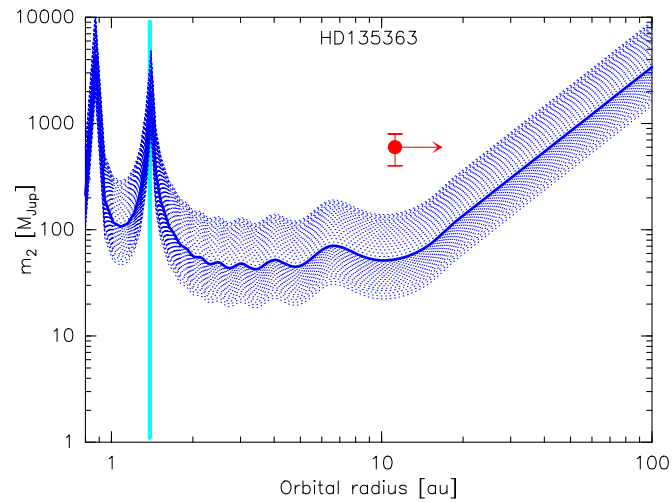


Figure 14. Same as Figure 11, but for HD 135363. The red circle marks the parameters of the known visual companion WDS 09035+3750 B.

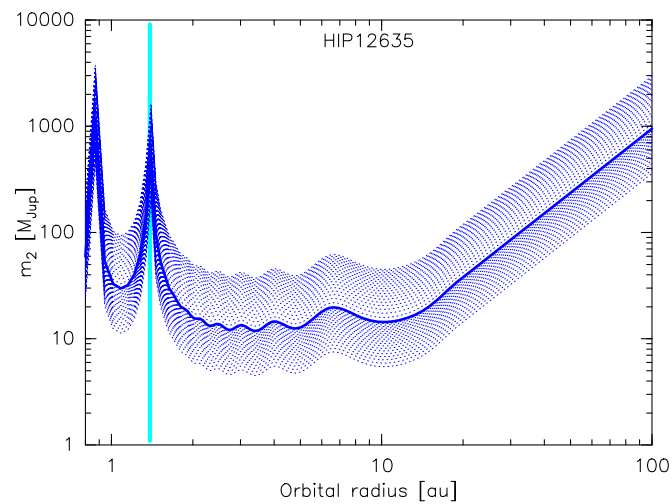


Figure 15. Same as Figure 11, but for HIP 12635. There is no known companion that could explain the observed PMa.

ORCID iDs

Ralf Launhardt  <https://orcid.org/0000-0002-8298-2663>
 Laurent Loinard  <https://orcid.org/0000-0002-5635-3345>
 Sergio A. Dzib  <https://orcid.org/0000-0001-6010-6200>
 Jan Forbrich  <https://orcid.org/0000-0001-8694-4966>
 Geoffrey C. Bower  <https://orcid.org/0000-0003-4056-9982>
 Thomas K. Henning  <https://orcid.org/0000-0002-1493-300X>
 Sabine Reffert  <https://orcid.org/0000-0002-0460-8289>

References

- Adams, F. C., Lada, C. J., & Shu, F. H. 1987, *ApJ*, 312, 788
 Allard, F. 2014, in IAU Symp. 299, Exploring the Formation and Evolution of Planetary Systems (Cambridge: Cambridge Univ. Press), 271
 André, P., Montmerle, T., & Feigelson, E. D. 1987, *AJ*, 93, 1182
 Anglada, G., Rodríguez, L. F., Canto, J., Estalella, R., & Torrelles, J. M. 1992, *ApJ*, 395, 494
 Anglada, G., Rodríguez, L. F., & Carrasco-González, C. 2018, *A&ARv*, 26, 3
 Bailer-Jones, C. A. L., Rybizki, J., Fousneau, M., Mantelet, G., & Andrae, R. 2018, *AJ*, 156, 58
 Baraffe, I., Homeier, D., Allard, F., & Chabrier, G. 2015, *A&A*, 577, A42
 Bell, C. P. M., Mamajek, E. E., & Naylor, T. 2015, *MNRAS*, 454, 593
 Benz, A. O., & Güdel, M. 1994, *A&A*, 285, 621
 Binks, A. S., & Jeffries, R. D. 2016, *MNRAS*, 455, 3345
 Boller, T., Freyberg, M. J., Trümper, J., et al. 2016, *A&A*, 588, A103
 Bouvier, J., Matt, S. P., Mohanty, S., et al. 2014, in Protostars and Planets VI, ed. H. Beuther et al. (Tucson, AZ: Univ. Arizona Press), 433
 Bower, G. C., Bolatto, A., Ford, E. B., & Kalas, P. 2009, *ApJ*, 701, 1922
 Bowler, B. P., Liu, M. C., Shkolnik, E. L., & Tamura, M. 2015, *ApJS*, 216, 7
 Brandt, T. D., & Huang, C. X. 2015, *ApJ*, 807, 58
 Brandt, T. D., McElwain, M. W., Turner, E. L., et al. 2014, *ApJ*, 794, 159
 Carpenter, J. M., Bouwman, J., Mamajek, E. E., et al. 2009, *ApJS*, 181, 197
 Condon, J. J., Cotton, W. D., Greisen, E. W., et al. 1998, *AJ*, 115, 1693
 Curiel, S., Ortiz-León, G. N., Mioduszewski, A. J., & Torres, R. M. 2020, *AJ*, 160, 97
 Cutri, R. M., Wright, E. L., Conrow, T., et al. 2012, WISE All-Sky Source Catalog, doi:10.26131/IRSA142
 da Silva, L., Torres, C. A. O., de La Reza, R., et al. 2009, *A&A*, 508, 833
 Dahm, S. E. 2015, *ApJ*, 813, 108
 David, T. J., & Hillenbrand, L. A. 2015, *ApJ*, 804, 146
 Deller, A. T., Forbrich, J., & Loinard, L. 2013, *A&A*, 552, A51
 Desidera, S., Chauvin, G., Bonavita, M., et al. 2021, *A&A*, 651, A70
 Desidera, S., Covino, E., Messina, S., et al. 2015, *A&A*, 573, A126
 Dulk, G. A. 1985, *ARA&A*, 23, 169
 Dzib, S., Loinard, L., Mioduszewski, A. J., et al. 2010, *ApJ*, 718, 610
 Dzib, S. A., Forbrich, J., Reid, M. J., & Menten, K. M. 2021, *ApJ*, 906, 24
 Dzib, S. A., Loinard, L., Mioduszewski, A. J., et al. 2013, *ApJ*, 775, 63
 Dzib, S. A., Loinard, L., Rodríguez, L. F., et al. 2015, *ApJ*, 801, 91
 ESA 1997, in ESA Special Publication 1200, The HIPPARCOS and TYCHO Catalogues (Noordwijk: ESA)
 Eislöffel, J., Mundt, R., Ray, T. P., & Rodríguez, L. F. 2000, in Protostars and Planets IV, ed. V. Mannings et al. (Tucson, AZ: Univ. Arizona Press), 815
 Evans, T. M., Ireland, M. J., Kraus, A. L., et al. 2012, *ApJ*, 744, 120
 Feigelson, E. D., & Montmerle, T. 1985, *ApJL*, 289, L19
 Fomalont, E. B., Windhorst, R. A., Kristian, J. A., & Kellerman, K. I. 1991, *AJ*, 102, 1258
 Forbrich, J., Dzib, S. A., Reid, M. J., & Menten, K. M. 2021, *ApJ*, 906, 23
 Forbrich, J., Reid, M. J., Menten, K. M., et al. 2017, *ApJ*, 844, 109
 Forbrich, J., Rivilla, V. M., Menten, K. M., et al. 2016, *ApJ*, 822, 93
 Gagné, J., Mamajek, E. E., Malo, L., et al. 2018, *ApJ*, 856, 23
 Gaia Collaboration, Brown, A. G. A., Vallenari, A., et al. 2018, *A&A*, 616, A1
 Galicher, R., Marois, C., Macintosh, B., et al. 2016, *A&A*, 594, A63
 Gáspár, A., Rieke, G. H., & Ballering, N. 2016, *ApJ*, 826, 171
 Getman, K. V., & Feigelson, E. D. 2021, *ApJ*, 916, 32
 Güdel, M. 2002, *ARA&A*, 40, 217
 Güdel, M. 2004, *A&ARv*, 12, 71
 Güdel, M. 2020, *SSRv*, 216, 143
 Güdel, M., & Benz, A. O. 1993, *ApJL*, 405, L63
 Høg, E., Fabricius, C., Makarov, V. V., et al. 2000, *A&A*, 355, L27
 Holmberg, J., Nordström, B., & Andersen, J. 2009, *A&A*, 501, 941
 Husser, T.-O., Wende-von Berg, S., Dreizler, S., et al. 2013, *A&A*, 553, A6
 Kammerer, J., Ireland, M. J., Martinache, F., & Girard, J. H. 2019, *MNRAS*, 486, 639
 Kenyon, S. J., & Hartmann, L. 1995, *ApJS*, 101, 117
 Kervella, P., Arenou, F., Mignard, F., & Thévenin, F. 2019, *A&A*, 623, A72
 Kounkel, M., Hartmann, L., Loinard, L., et al. 2014, *ApJ*, 790, 49
 Kounkel, M., Hartmann, L., Loinard, L., et al. 2017, *ApJ*, 834, 142
 Lada, C. J. 1987, in IAU Symp. 115, Star Forming Regions, ed. M. Pembert & J. Jugaku (Dordrecht: Reidel), 1
 Launhardt, R., Henning, T., Quirrenbach, A., et al. 2020, *A&A*, 635, A162
 Lindegren, L., Hernández, J., Bombrun, A., et al. 2018, *A&A*, 616, A2
 Loinard, L., Mioduszewski, A. J., Torres, R. M., et al. 2011, *RMxAC*, 40, 205
 López-Santiago, J., Montes, D., Crespo-Chacón, I., & Fernández-Figueroa, M. J. 2006, *ApJ*, 643, 1160
 Maldonado, J., Martínez-Arnáiz, R. M., Eiroa, C., Montes, D., & Montesinos, B. 2010, *A&A*, 521, A12
 Mason, B. D., Wycoff, G. L., Hartkopf, W. I., Douglass, G. G., & Worley, C. E. 2020, *yCat*, B/wds
 Massi, M., Forbrich, J., Menten, K. M., et al. 2006, *A&A*, 453, 959
 Meyer, M. R., Hillenbrand, L. A., Backman, D., et al. 2006, *PASP*, 118, 1690
 Montes, D., López-Santiago, J., Gálvez, M. C., et al. 2001, *MNRAS*, 328, 45
 Montes, D., López-Santiago, J., Martínez-Arnáiz, R. M., et al. 2009, in AIP Conf. Ser. 1094, 15th Cambridge Workshop on Cool Stars, Stellar Systems, and the Sun, ed. E. S. Stempels (Melville, NY: AIP), 943
 Nakajima, T., & Morino, J.-I. 2012, *AJ*, 143, 2
 Nielsen, E. L., De Rosa, R. J., Macintosh, B., et al. 2019, *AJ*, 158, 13
 Ortiz-León, G. N., Loinard, L., Mioduszewski, A. J., et al. 2015, *ApJ*, 805, 9
 Ortiz-León, G. N., Loinard, L., Kounkel, M. A., et al. 2017a, *ApJ*, 834, 141
 Ortiz-León, G. N., Dzib, S. A., Kounkel, M. A., et al. 2017b, *ApJ*, 834, 143
 Paturel, G., Fouque, P., Bottinelli, L., & Gouguenheim, L. 1995, *yCat*, VII/119
 Pearce, T. D., Launhardt, R., Ostermann, R., et al. 2022, *A&A*, 659, A135
 Pecaut, M. J., & Mamajek, E. E. 2013, *ApJS*, 208, 9
 Pech, G., Loinard, L., Dzib, S. A., et al. 2016, *ApJ*, 818, 116
 Pourbaix, D., Tokovinin, A. A., Batten, A. H., et al. 2004, *A&A*, 424, 727
 Skrutskie, M. F., Cutri, R. M., Stiening, R., et al. 2003, 2MASS All-Sky Point Source Catalog, doi:10.26131/IRSA2
 Smith, K., Pestalozzi, M., Güdel, M., Conway, J., & Benz, A. O. 2003, *A&A*, 406, 957
 Stanford-Moore, S. A., Nielsen, E. L., De Rosa, R. J., Macintosh, B., & Czekala, I. 2020, *ApJ*, 898, 27
 Stothers, R., & Frogel, J. A. 1974, *AJ*, 79, 456
 Torres, R. M., Loinard, L., Mioduszewski, A. J., et al. 2012, *ApJ*, 747, 18
 van Leeuwen, F. 2010, *SSRv*, 151, 209
 Weise, P., Launhardt, R., Setiawan, J., & Henning, T. 2010, *A&A*, 517, A88
 Wichmann, R., Schmitt, J. H. M. M., & Hubrig, S. 2003, *A&A*, 399, 983
 York, D. G., Adelman, J. A., John, E. J., et al. 2000, *AJ*, 120, 1579
 Zucker, C., Goodman, A. A., Alves, J., et al. 2022, *Natur*, 601, 334
 Zuckerman, B. 2019, *ApJ*, 870, 27
 Zuckerman, B., Bessell, M. S., Song, I., & Kim, S. 2006, *ApJL*, 649, L115
 Zuckerman, B., Rhee, J. H., Song, I., & Bessell, M. S. 2011, *ApJ*, 732, 61
 Zuckerman, B., & Song, I. 2004, *ApJ*, 603, 738